Ten3–Lphn2-mediated target selection across the extended hippocampal network demonstrates a repeated strategy for circuit assembly

Ellen C. Gingrich[1,2], Daniel T. Pederick[1,3], Yanbo Zhang[1], Liqun Luo[1]

[1]Department of Biology, Howard Hughes Medical Institute, Stanford University, Stanford, CA, 94305, USA
[2]Neurosciences Interdepartmental PhD Program, Stanford University, Stanford, CA, 94305, USA
[3]Present address: Department of Neuroscience, Johns Hopkins University, Baltimore, MD, USA

SUMMARY

How do a limited number of wiring molecules specify trillions of connections in developing brains? We previously found that inverse expression of a ligand–receptor pair, Teneurin-3 (Ten3) and Latrophilin-2 (Lphn2) in CA1 and subiculum instructs CA1→subiculum target selection through Ten3–Ten3 homophilic attraction and Ten3–Lphn2 heterophilic reciprocal repulsion. Here, we leveraged conditional knockouts to systematically demonstrate that these mechanisms generalize to extended hippocampal connections, including entorhinal cortex and hypothalamus. Cooperation between attraction and repulsion differs depending on the order developing axons encounter the attractant and repellent subfields. Strikingly, Ten3 and Lphn2 can serve both as ligands for incoming axons and receptors for their own target selection, within the same neuron; Ten3 can be repulsive or attractive as ligand or receptor. Thus, multifunctionality and repeated use, together with the recurrent circuit motifs prevalent in the brain, enable one ligand–receptor pair to instruct target selection of many more neurons.

INTRODUCTION

During development, neural circuits must self-assemble with exquisite wiring precision to enable normal cognition and behavior, including functions such as memory and spatial navigation. Roger Sperry proposed in his chemoaffinity hypothesis that, to accomplish this feat, individual neurons carry unique molecular identification tags that report their identity to neighboring cells.[1] In the intervening years, many such cell-surface proteins (CSPs) have been identified as critical regulators of axon guidance and target selection.[2,3] These CSPs can be expressed on both pre- and post-synaptic cells and use mechanisms of attraction and repulsion to specify neuronal partner matching.[4–13]

The human brain, however, contains ~10^{11} neurons, each making thousands of synaptic connections, but fewer than 3000 CSPs that can be leveraged to guide wiring.[14–17] This presents a challenge to the developing brain, as the number of connections to specify vastly outnumbers the genes available to instruct them, precluding the possibility that each neuron carries a unique tag. Among multiple strategies that have been proposed to overcome this discrepancy, one is to re-use the same CSPs at spatially distinct locations.[18] For example, the ligand–receptor pair, ephrin-A–EphA, have inverse expression in several retinotopic nodes of the visual circuit including the retina, superior colliculus (SC), lateral geniculate nucleus (LGN), and the primary visual cortex (V1).[19] In the retina→SC connection, ephrin-A–EphA-mediated reciprocal repulsion during target selection has been shown to establish the precise anterior–posterior retinotopy.[5,6,20–25] However, although ephrin-A–EphA signaling is hypothesized to directly regulate retinotopic connectivity across subsequent nodes, this has not been extensively studied beyond how retina→SC mis-wiring can effect downstream visual circuitry.[26] Additionally, there is a shortage of tissue-specific loss-of-function studies that interrogate the roles of ephrin-A and EphA in axons and targets independently to distinguish pre- versus post-synaptic effects. Indeed, one of the few conditional manipulations done uncovered the importance of target-independent axon-axon interactions in establishing retinocollicular connectivity. [27]

Another circuit with well-characterized topographic projections across multiple nodes is the extended hippocampal network (Figure 1A). The medial and lateral hippocampal subnetworks (MHN and LHN) appear to preferentially process spatial and object-related information, respectively.[28,29] The MHN consists, in part, of

proximal CA1 (pCA1), distal subiculum (dSub), medial entorhinal cortex (MEC), and lateral subdivision of the medial mammillary nucleus (lat-mMN) of the hypothalamus, which are interconnected with each other. Conversely, the LHN consists of interconnected distal CA1 (dCA1), proximal subiculum (pSub), lateral entorhinal cortex (LEC), and medial mMN (med-mMN) (Figure 1A).[30–36]

We previously found a CSP pair, teneurin-3 (Ten3) and latrophilin-2 (Lphn2), that exhibit striking inverse expression in both CA1 and subiculum, such that the interconnected regions of pCA1→dSub and dCA1→pSub express Ten3 and Lphn2, respectively (Figure 1A).[10,11] Genetic loss- and gain-of-function analyses revealed that the CA1→subiculum specificity is produced through cooperation between homophilic Ten3–Ten3-mediated attraction and heterophilic Ten3–Lphn2-mediated reciprocal repulsions.[11,37] Given that Ten3 and Lphn2 also exhibit inverse expression in other nodes of the MHN and LHN including entorhinal cortex (EC) and medial mammillary nucleus (mMN),[10,11,38,39] here we address whether other parts of the network follow a 'Ten3→Ten3, Lphn2→Lphn2' connectivity rule and, if so, whether this ligand–receptor pair is used repeatedly to instruct the precise assembly at other nodes of the circuit using systematic conditional knockout analyses.

RESULTS

The extended hippocampal network follows a 'Ten3→Ten3, Lphn2→Lphn2' connectivity rule

Beyond its inverse and topographic expression in CA1 and subiculum, Ten3 is also enriched in subregions of several other nodes in the extended hippocampal network, including MEC and lat-mMN.[10,39] Conversely, Lphn2 is known to be enriched in LEC (Figure 1A).[11,38,39] Immunostaining for tagged Ten3 and Lphn2 (in *Ten3*$^{HA/HA}$*;Lphn2*$^{mV/mV}$ animals[40]) confirmed the striking inverse expression of these two proteins at postnatal day 8 (P8). As previously reported, Ten3 protein is enriched in pCA1, dSub, MEC, and lat-mMN; by contrast, Lphn2 protein is enriched in dCA1, pSub, LEC, and med-mMN (Figure 1A, B).[10,11,38] Given this topographically-restricted expression, we considered whether these two CSPs may serve a broader role in assembling the extended hippocampal networks than previously appreciated.

Previous studies have focused on the relationship between Ten3–Lphn2 inverse expression and connection topography in the hippocampal-entorhinal circuitry.[10,11,38] To further investigate this relationship, specifically in hippocampal outputs to hypothalamus, we injected adeno-associated viruses (AAVs) as anterograde tracers into neighboring locations in subiculum (*AAV-GFP* into Lphn2-high pSub, *AAV-mCherry* (*mCh*) into Ten3-high dSub) and assessed their projections to mMN (Figure 1C$_1$, Figure SA$_1$). Note that in this study, pSub will refer to the entirety of the Lphn2-high region of subiculum which anatomically constitutes approximately 75% of the length of subiculum (Figure SA$_1$).[11] We found that GFP$^+$ axons were restricted to Lphn2-high med-mMN whereas mCh$^+$ axons filled Ten3-high lat-mMN (Figure 1C$_2$, Figure SA$_2$, B), validating that the 'Ten3→Ten3, Lphn2→Lphn2' connectivity rule also applies to subiculum→mMN projection, analogous to projections between CA1, subiculum, and entorhinal cortex (Figure 1A).[10,11] The axons from subiculum to mMN, however, did not appear to be topographically segregated, instead forming a uniform bundle that only splits into the appropriate subfield as it enters the mMN target region (Figure S1B).

Spatiotemporal patterns of Ten3 and Lphn2 expression with respect to target entry of developing axons

To instruct target selection of axons connecting these nodes, Ten3 and Lphn2 must be inversely expressed at each node prior to the maturation of the circuit. To establish expression onset, we performed dual in situ hybridization for *Ten3* and *Lphn2* mRNA using RNAScope[41] across multiple developmental timepoints. At E15.5, *Ten3* and *Lphn2* were already inversely expressed in mMN (Figure 1E) but exhibited very low expression in the hippocampal and entorhinal regions. By E17.5, *Ten3* was highly expressed in entorhinal cortex whereas *Lphn2* expression remained low, marking this as the only case we observed where *Ten3–Lphn2* were not inversely expressed at onset (Figure 1D$_1$). By P0, CA1, subiculum, and entorhinal cortex all exhibited inverse expression, resembling protein staining at P8 and in previous studies (Figure 1B$_1$, D$_2$).[11,39] *Ex vivo* tracing from MEC showed that axons began to invade dSub at E17.5 and increased in density through P0, roughly aligning with the onset of *Ten3* and *Lphn2* expression in dSub and pSub, respectively (Figure S1C, D). Although little is known about the

timing of subiculum→mMN axon targeting, expression of *Ten3* and *Lphn2* in the subiculum axon bundle indicated these axons reach mMN around P0.[40] Since each node of the circuit expressed *Ten3* and *Lphn2* mRNA (Figure 1D, E), the protein distribution we observed (Figure 1B) is likely contributed to by both axons and targets, further reinforcing the prevalence of like–like connectivity.

Although each of the four nodes we examined—CA1, subiculum, entorhinal cortex, and mMN—exhibited striking inverse expression of Ten3 and Lphn2, the spatial arrangement of developing axons encountering each target node in relation to the expression pattern could influence target selection strategy. By re-examining our previous study,[10] characterizing adult axon entry routes,[42–44] performing developmental tracing, and cataloguing Ten3–Lphn2 protein expression, we established three distinct spatial configurations in which axons may encounter Ten3 and Lphn2 subregions in the target (Figure 1F; Figure S1B, E–G). (1) For CA1→subiculum at P2, Ten3$^+$ pCA1 axons first encounter the Lphn2$^+$ pSub, then encounter Ten3$^+$ dSub (Figure 1F, left)[10], consistent with adult single axon tracing studies.[43,44] (2) For entorhinal cortex→subiculum, Ten3$^+$ MEC axons first encounter the Ten3$^+$ dSub, then Lphn2$^+$ pSub, as apparent in *ex vivo* tracing of MEC in P0 *Ten3$^{HA/HA}$;Lphn2$^{mV/mV}$* pups (Figure 1F, middle; Figure S1E). This is also consistent with adult single axon tracing from entorhinal cortex.[42,45,46] (3) For subiculum→mMN, Ten3$^+$ dSub axons encounter the Ten3$^+$ lat-mMN and Lphn2$^+$ med-mMN subfields simultaneously, confronting them with a more binary choice (Figure 1F, right; Figure S1B, F, G). Our previous work has established that both Ten3–Ten3 homophilic attraction and Ten3–Lphn2 heterophilic reciprocal repulsion are critical in the first scenario (Figure 1F, left). However, it remains unclear how the other two configurations of developing axons encountering the Ten3$^+$ or Lphn2$^+$ target subfields (Figure 1F, middle and right) may influence the use of these mechanisms.

In the rest of this study, we carried out systematic conditional knockout (cKO) experiments to determine whether Ten3 and Lphn2 are reused for target selection in the extended hippocampal network, and whether variations in how axons encounter the spatial configurations of Ten3 and Lphn2 in targets influence their use. We first examined the MEC (Ten3$^+$)→dSub (Ten3$^+$) connection.

Ten3 is required in MEC axons for their precise targeting to dSub

Ten3–Ten3 homophilic attraction and Lphn2–Ten3 heterophilic repulsion are critical for establishing the appropriate topography of the pCA1→dSub connection.[11] To determine if these mechanisms are re-used at the MEC→dSub connection, we first asked if Ten3 is required in MEC axons using a conditional knockout strategy. We injected *Cre-GFP*-expressing lentivirus into postnatal day 0 (P0) wildtype or *Ten3$^{fl/fl}$* pups, titrating the concentration to allow for a roughly even proportion of Cre$^+$ and Cre$^-$ neurons in MEC (Figure 2A, left). At P42 or older, we injected a mix of anterograde *AAV-CreON-GFP* and *AAV-CreOFF-mCh* into MEC of these mice (Figure 2A, middle) to assess the targeting of control and *Ten3*-null axons within the same animal (Figure 2A, right). Injections were restricted to within the most medial 20% of entorhinal cortex to ensure tracing of mostly Ten3$^+$ axons (Figure 2B).

In *Ten3$^{+/+}$* controls, mCh$^+$ (Cre$^-$) and GFP$^+$ (Cre$^+$) MEC neurons alike exclusively projected to the distal, Ten3-high region of the subiculum (Figure 2C, D, G). However, in *Ten3$^{fl/fl}$* mice, mCh$^+$ axons (Cre$^-$, functionally wildtype) remained restricted to Ten3-high dSub, whereas GFP$^+$ (Cre$^+$, *Ten3* conditionally knocked out, or *Ten3^{MEC}-cKO*) axons invaded Lphn2-high regions of pSub (Figure 2E, F, H). Quantification of axon fluorescence intensity (FI) showed that only GFP$^+$ axons in *Ten3$^{fl/fl}$* mice had a proximal shift along the distal–proximal axis of the subiculum (Figure 2G$_1$, H$_1$). This shift resulted in lower axon density in the appropriate Ten3-high dSub and increased density in the Lphn2-high pSub (Figure 2G$_2$, H$_2$). This mistargeting also caused GFP$^+$ axons to cover a larger region of subiculum, as evidenced by area under the curve of FI traces, when Cre$^-$ and Cre$^+$ projections were compared pairwise within animals (Figure 2I). A similar phenotype was observed for target selection of MEC axons in CA1: GFP$^+$ (and *Ten3^{MEC}-cKO*) axons in *Ten3$^{fl/fl}$* mice spread more distally into Lphn2-high regions compared to mCh$^+$ wildtype axons (Figure S2A–D).

MEC axons also have topographic projections to contralateral dSub and pCA1 that could be affected by *Ten3^{MEC}-cKO*. Although these projections are much sparser than the ipsilateral connection and were not observable in every animal, qualitatively, GFP$^+$ axons also mistargeted into Lphn2-high regions of pSub and

dCA1 in *Ten3*$^{fl/fl}$ mice compared to mCh^{+} axons in *Ten3*$^{fl/fl}$ mice or GFP^{+} and mCh^{+} axons in *Ten3*$^{+/+}$ control mice (Figure 2K, L; Figure S2F). Taken together, these data demonstrated that Ten3 is required in MEC neurons for their axons to precisely target to dSub and pCA1 (Figure 2J, M; Figure S2E, G).

Ten3 and Lphn2 in subiculum cooperate to instruct the precise targeting of MEC axons

Given that Ten3 is required in MEC axons for target selection in subiculum, next we asked whether Ten3 and/or Lphn2 are required in the subiculum target. We used a pan-subiculum Cre driver, *Nts-Cre*, with dense expression in subiculum at P0 (Figure 3A; Figure S3A) but minimal expression in entorhinal cortex or CA1 (Figure S3A, B), to conditionally knockout *Ten3*, *Lphn2*, or both in subiculum but not in entorhinal cortex or CA1.

We injected *AAV-CreOFF-mCh* into MEC to assess MEC→dSub axon projections (Figure 3B, C). To examine if target deletions could recapitulate the same phenotype as seen in *Ten3*^{MEC}*-cKO* (which presumably lose both Ten3–Ten3 attraction and Lphn2–Ten3 repulsion; Figure 2H), we started by assessing *Ten3* and *Lphn2* double cKO mice. In *Nts-Cre;Ten3*$^{fl/fl}$*;Lphn2*$^{fl/fl}$ (*Ten3*^{Sub}*/Lphn2*^{Sub}-cKO) mice, we observed mistargeting of Ten3^{+} axons into the Lphn2-high subregion of subiculum compared to *Ten3*$^{fl/fl}$*;Lphn2*$^{fl/fl}$ littermate controls (Figure 3D–G). By contrast, we did not observe mistargeting of MEC→pCA1 axon in the same experiment (Figure S4A–C), as would be expected since *Nts-Cre* is not expressed in CA1 and thus Ten3 and Lphn2 were still normally expressed in both axons and target of this connection. These experiments demonstrated that Ten3 and/or Lphn2 are required in the subiculum target for Ten3^{+} MEC axons to target to Ten3^{+} dSub, through Ten3–Ten3 homophilic attraction, Lphn2–Ten3 heterophilic repulsion, or a combination.

To examine the relative contribution of Ten3–Ten3 homophilic attraction and Lphn2–Ten3 heterophilic repulsion, we repeated these experiments with single cKOs: (1) *Nts-Cre;Lphn2*$^{fl/fl}$ (*Lphn2*^{Sub}-cKO; with *Nts-Cre;Lphn2*$^{+/+}$ littermate controls); and (2) *Nts-Cre;Ten3*$^{fl/fl}$ (*Ten3*^{Sub}-cKO; with *Nts-Cre;Ten3*$^{+/+}$ littermate controls). As expected, CA1 targeting was normal under both conditions (Figure S4D, E). Unexpectedly, however, Ten3^{+} MEC axons appeared to target the appropriate subiculum region in both single knockout conditions (Figure 3H–K).

These data suggest that Ten3–Ten3-mediated attraction and Lphn2–Ten3-mediated repulsion are redundant; each mechanism can compensate for the loss of the other (Figure 3L). This is contrary to our previous studies of pCA1→dSub targeting, where conditional knockout of either *Ten3* (attraction) or *Lphn2* (repulsion) in the subiculum target produces severe mistargeting phenotypes.[10,11] One possibility is that unlike the pCA1→dSub projection, where axons must traverse a large Lphn2-high region of pSub before contacting the appropriate dSub target, in the MEC→dSub projection, MEC axons encounter the Ten3 attractant first (Figure 1F, Figure S1E), such that attraction alone may stabilize MEC axons before they reach the Lphn2-high pSub. Lphn2 expression may provide a safety gate to restrict growth. When both Ten3 and Lphn2 are removed from the target, MEC axons behave similarly to removing Ten3 from MEC neurons, supporting that Ten3–Ten3 attraction and Lphn2–Ten3 repulsion cooperate in mediating MEC→dSub target selection.

Ten3 is required in subiculum for dSub axons to precisely target to lateral mMN

The precise targeting of pCA1→dSub and MEC→dSub both require the cooperation of Ten3–Ten3 attraction and Lphn2–Ten3 repulsion, but differ in their degree of reliance on these mechanisms individually. Next, we asked if these mechanisms generalize to a third scenario: axons encountering Ten3 and Lphn2 concurrently, as seen in dSub→lat-mMN connection (Figure 1F; Figure S1F, G).

Using the same *Nts-Cre* driver as above, first we assessed if Ten3 is required in dSub axons for appropriate targeting to lat-mMN by injecting *AAV-CreON-mCh* into dSub of *Nts-Cre;Ten3*$^{+/+}$ controls and *Nts-Cre;Ten3*$^{fl/fl}$ (*Ten3*^{Sub}-cKO) mice (Figure 4A, B). Note that unlike in Figure 3, where *Ten3*^{Sub}-cKO was used to examine the consequence of <u>target</u> deletion for MEC→dSub projection, hereafter we used *Ten3*^{Sub}-cKO to examine the consequence of <u>axon</u> deletion for subiculum→mMN projection. In control animals, dSub axons were restricted to the Ten3-high lateral region of mMN (lat-mMN; Figure 4C, D). However, dSub axons in *Ten3*^{Sub}-cKO animals began to spread into Lphn2-high med-mMN (Figure 4E, F). Because the mMN cannot be easily approximated as a linear structure, like hippocampal or entorhinal regions, we quantified axon mistargeting by defining the lat-

mMN and med-mMN boundaries using DAPI counterstaining and calculating the ratio of total fluorescence intensity within each. In control animals, axons were predominantly restricted to the lat-mMN, whereas in *Ten3*^{Sub}-cKO, the ratio of axons in med-mMN increased with a concurrent decrease in lat-mMN (Figure 4G).

Even in an independent cohort of animals with relatively weaker and more distally restricted injection sites (Figure S5A, C, E), individual aberrant axons can be seen straying outside of lat-mMN into Lphn2-high med-mMN in *Ten3*^{Sub}-cKO animals relative to controls (Figure S5B, D). Rather than a regional analysis, these animals were rank-ordered by severity of mistargeting by an by an independent researcher blinded to genotype. This analysis showed that the ranks of control and *Ten3*^{Sub}-cKO mMN were statistically different, with *Ten3*^{Sub}-cKO animals consistently ranked as having more mistargeting (Figure S5F$_1$). This sparse labeling of *Ten3*-null axons showed that individual axons could mistarget as far as the most anterior-medial border of med-mMN (i.e., the Lphn2-high region furthest from Ten3-high lat-mMN) and did not exclusively mistarget to the bordering Lphn2-high subfield, as seen in MEC→dSub. We also observed this dSub axonal spread to med-mMN as these projections cross the midline into contralateral mMN, suggesting that once the targeting is disrupted, the axons remain in the incorrect subdomain (Figure 4I; Figure S5F$_2$). These data indicate that Ten3 is required in dSub axons to precisely target lat-mMN (Figure 4H).

Lphn2 is required in mMN for the precise targeting of dSub axons to lat-mMN

Given that Ten3 is required in dSub axons to appropriately target to mMN as it is in the pCA1→dSub and MEC→dSub connections, we asked whether *Ten3* and/or *Lphn2* are also the ligands required in the mMN target. To do this, we used *Sim1-Cre*, a Cre driver with dense expression in mMN as early as E15.5 (Figure 5A, Figure S3D), but minimal expression in subiculum (Figure S3E).

We injected *AAV-mCh* into dSub to assess dSub→lat-mMN axon projections and, again, started by assessing *Sim1-Cre;Ten3*$^{fl/fl}$*;Lphn2*$^{fl/fl}$ (*Ten3*^{mMN}*/Lphn2*^{mMN}-cKO) animals to determine if the Ten3 axonal deletion phenotype is recapitulated by *Ten3* and *Lphn2* double cKO in the target (Figure 5B, C). In *Ten3*^{mMN}*/Lphn2*^{mMN}-cKO animals, we observed mistargeting of the Ten3$^+$ dSub axons into the Lphn2-high med-mMN when compared to *Ten3*$^{fl/fl}$*;Lphn2*$^{fl/fl}$ control (Figure 5D–G). This mistargeting was also observed in contralateral mMN of *Ten3*^{mMN}*/Lphn2*^{mMN}-cKO (Figure S6A, B). This experiment demonstrated that Ten3 and/or Lphn2 is required in mMN for the appropriate targeting of Ten3$^+$ dSub axons.

To determine the relative contribution of Lphn2 and Ten3 to the double target knockout phenotype, we repeated these experiments with *Lphn2* or *Ten3* single cKOs in the mMN target. As in *Ten3*^{mMN}*/Lphn2*^{mMN}-cKO, Ten3$^+$ dSub axons mistargeted to med-mMN in *Lphn2*^{mMN}-cKO animals, causing an increase in the density of axons in med-mMN relative to the appropriate lat-mMN target (Figure 5H, I). However, dSub axons in *Ten3*^{mMN}-cKO still predominantly targeted lat-mMN (Figure 5J, K). These phenotypes were recapitulated in contralateral mMN with mistargeting in *Lphn2*^{mMN}-cKO, but not *Ten3*^{mMN}-cKO animals (Figure S6C, D).

Taken together, these results suggested that Lphn2–Ten3-mediated repulsion is required in the dSub→lat-mMN connection (Figure 5L, Figure S6E). Additionally, the mistargeting phenotype in *Lphn2*^{mMN}-cKO animals implied that, like in pCA1→dSub, Ten3-mediated attraction alone cannot compensate for the loss of Lphn2-mediated repulsion for the appropriate targeting of Ten3$^+$ axons.

Lphn2 is required in subiculum for precise targeting of pSub axons to med-mMN

So far, we have focused on connections between target selection of Ten3$^+$ axons in the medial subdivision of the hippocampal network (Figure 1A). However, in the dCA1→pSub (the lateral subregions of the CA1→subiculum connection), Lphn2$^+$ CA1 axons are repelled by Ten3 in dSub, meaning Ten3–Lphn2 heterophilic repulsions are reciprocal, with both Ten3 and Lphn2 capable of acting as receptor and ligand.[11] Therefore, we asked whether reciprocal repulsions are also generalizable to other nodes in the extended hippocampal network. We used pSub→med-mMN, the Lphn2-high subdivision of the subiculum→mMN connection, to address this question.

Modifying the experiments in Figure 4 for examining Lphn2$^+$ axons, we injected *AAV-CreON-GFP* into pSub of *Nts-Cre;Lphn2*$^{+/+}$ controls and *Nts-Cre;Lphn2*$^{fl/fl}$ (*Lphn2*^{Sub}-cKO) mice (Figure 6A, B). In control animals, pSub axons were restricted to the med-mMN whereas aberrant pSub axons strayed into lat-mMN in

Lphn2^{Sub}-cKO (Figure 6C–F). Although this phenotype was more subtle than when *Ten3* was deleted in dSub axons, there was a significant reduction in axon density in the appropriate med-mMN target and concomitant increase in Ten3-high lat-mMN (Figure 6G). This phenotype was also present in contralateral mMN (Figure 6I). These data demonstrate that Lphn2 is required in subiculum for pSub axons to precisely target med-mMN (Figure 6H).

Target requirement for the pSub→med-mMN projection

To determine if Ten3–Lphn2 are required in the mMN target for the appropriate targeting of pSub→med-mMN and, thus, recapitulate the *Lphn2*^{Sub}-cKO phenotype, we injected *AAV-GFP* into pSub of *Sim1-Cre;Ten3*$^{fl/fl}$*;Lphn2*$^{fl/fl}$ (*Ten3*^{mMN}*/Lphn2*^{mMN}-cKO) animals (Figure 7A, B). Indeed, in *Ten3*^{mMN}*/Lphn2*^{mMN}-cKO animals, we observed aberrant Lphn2^{+} pSub axons in the Ten3-high lat-mMN when compared to *Ten3*$^{fl/fl}$*;Lphn2*$^{fl/fl}$ controls (Figure 7C–G), including in contralateral mMN (Figure 7I). This recapitulated the phenotype of *Lphn2* deletion in subiculum axons (Figure 6). Because Lphn2 does not exhibit homophilic binding,[11,47] we did not test single cKOs as it is unlikely that loss of Lphn2 in the target is contributing to the phenotype in *Ten3*^{mMN}*/Lphn2*^{mMN}-cKOs.

Taken together these data suggest that Ten3–Lphn2 heterophilic repulsion is required to correctly specify pSub→med-mMN (Figure 7H) and that this repulsion is reciprocal within the subiculum→mMN connection, as in the CA1→subiculum connection.

Lack of evidence that Ten3–Lphn2 mediates axon-axon interaction

Ligand–receptor pairs could mediate axon-axon interactions in addition to axon-target interaction.[27,48] Because we found that both Ten3^{+} and Lphn2^{+} axons from subiculum could serve as repulsive receptors for their respective ligand in the mMN, we asked whether these molecules could also mediate axon-axon repulsion, which could, in principle, sort Ten3^{+} dSub axons and Lphn2^{+} pSub axons prior to reaching the mMN target, which might contribute to precise target selection of these two population of axons. To do this, we traced Lphn2^{+} axons from pSub into their mMN target in *Ten3*^{Sub}-cKO animals to determine if loss of *Ten3* on neighboring axons effected their targeting (Figure S7A, F). We saw no difference in control and *Ten3*^{Sub}-cKO animals; in both cases, Lphn2^{+} pSub axons targeted to med-mMN appropriately, with no aberrant axons in lat-mMN (Figure S7B–E, G). These data argue against direct interaction between dSub and pSub axons playing a role in target selection at mMN (Figure S7H), and is consistent with our finding that dSub and pSub axons were intermingled prior to arrival at mMN, both in developing and adult brains (Figure S1B, F, G). These data also provide strong support that the phenotypes we observed in Figures 4–7 are due to interactions occurring exclusively in the target.

DISCUSSION

Here, we use the topographic connections of the extended hippocampal network to examine whether the same ligand–receptor pair can be re-used for target selection at multiple nodes of the same circuit. Our systematic conditional knockout approach demonstrated that Ten3–Ten3 homophilic attraction and Ten3–Lphn2 heterophilic reciprocal repulsion cooperate to specify several connections within the extended hippocampal network—MEC→dSub/pCA1, dSub→lat-mMN, and pSub→med-mMN, in addition to previously reported CA1→subiculum connections.[10,11] To our knowledge, this is the first time a ligand–receptor pair has been shown to instruct target selection in multiple nodes of the same network. Our analysis of conditional target deletions also revealed differential requirements of repulsion and attraction in different nodes depending on the order in which developing axons encounter the attractant versus the repellent subfield in the target (Figure 1F).

Differential requirement of attraction and repulsion at different circuit nodes

In the pCA1→dSub connection, our previous studies indicated that target deletion of *Lphn2* alone caused spread of pCA1 axons to pSub, and target deletion of both *Lphn2* and *Ten3* exhibited more severe pCA1 axon spreading to pSub.[11] Thus, Lphn2–Ten3 repulsion is by itself required for preventing pCA1 axon mistargeting. This makes

sense given that Ten3$^+$ pCA1 axons first encounter the Lphn2$^+$ pSub subfield before Ten3$^+$ dSub subfield (Figure 1F, left), making repulsion necessary to prevent axons stalling before they find the attractive subfield.

By contrast, our data indicates that conditional target deletion of *Lphn*2 did not cause significant targeting defect in the MEC→dSub connection (Figure 3I). Only when we deleted both *Ten3* and *Lphn2* in the subiculum target did we recapitulate *Ten3* deletion in MEC axon (Figure 3G, compared to Figure 2H). (Subiculum deletion of *Ten3* and *Lphn2* has a slightly weaker phenotype than *Ten3* deletion in MEC axons possibly due to late onset of *Nts-Cre,* between E17.5 and P0, such that some target proteins could have already been produced before conditional gene knockout.) Our developmental axon tracing indicated that MEC axons first encountered Ten3$^+$ dSub before encountering Lphn2$^+$ pSub (Figure 1F, middle; Figure S1D, E). Thus, the simplest interpretation for the lack of phenotype of *Lphn2* target deletion in the MEC→dSub connection is that Ten3–Ten3 homophilic attraction is sufficient to retain MEC axons in the Ten3$^+$ dSub subfield. Repulsion here provides a safety backup to increase the robustness of the system—only when attraction is disrupted would the importance of repulsion manifests itself.

Interestingly, when Ten3+ axons simultaneously encounter the Ten3$^+$ and Lphn2$^+$ target subfields, as is the case for the dSub→lat-mMN connection (Figure 1F, right; Figure S1F, G), conditional target deletion of *Lphn2* alone caused a robust mistargeting phenotype of Ten3$^+$ dSub axons entering the Lphn2$^+$ med-mMN subfield (Figure 5I). This indicates that Ten3–Ten3 attraction cannot compensate for the loss of Lphn2–Ten3 repulsion and highlights the importance of simultaneous push and pull in ensuring the correct axon sorting at the choice point. Altogether, these comparative analyses highlight the variations on the basic theme of cooperation between attraction and repulsion during target selection.

Incidentally, the order in which axons encounter the attractant versus repellent subfields also appears to influence the severity of mistargeting when it occurs. In *Ten3* and *Lphn2* double conditional target knockout, the MEC→dSub axons mistarget only to adjacent Lphn2-high regions (Figure 3), whereas dSub→lat-mMN axons can mistarget to the most medial region of med-mMN (Figure S5). Together, these data indicate the order in which axons encounter attractant and repellent subfields in the target is an important factor to consider in developmental studies.

Multi-functionality and repeated use highlight the economy of wiring molecules

Our study highlights two mechanisms that enable the developing brain to use a limited number of cell-surface recognition proteins to wire up many orders of magnitude more neurons and connections. The first mechanism is the multifunctionality of wiring molecules. Ten3 and Lphn2 can both serve as a ligand and a receptor. Ten3 can mediate both attraction and repulsion depending on its interacting partners and these roles can be simultaneously played within the same neuron. For example, in dSub neurons, Ten3 acts cell non-autonomously as an attractive ligand for MEC axons (Figure 3) and pCA1 axons,[10] and as a repulsive ligand for dCA1 axons.[11] and likely Lphn2$^+$ LEC axons (although this has not been directly tested). At the same time, it acts cell autonomously as a receptor for the Ten3 attractant and Lphn2 repellent in mMN as dSub axons select the appropriate subregion to make connections (Figure 4).

Similarly, Lphn2 in pSub neurons acts cell non-autonomously as a repulsive ligand for pCA1 axons.[11] as well as for MEC axons at least as a backup mechanism (Figure 3), while acting cell autonomously as a receptor for target selection in mMN (Figure 6). Such multifunctionality is both a result of the property of Ten3 and Lphn2 proteins as a ligand–receptor pair, as well as the circuit architecture of the extended hippocampal network, featuring convergent, divergent, and recurrent connectivity motifs.[49] Given the prevalence of these connectivity motifs in mammalian central nervous system, we envision that such multifunctionality of wiring molecules will become a theme when detailed functional analyses of wiring molecules like the current study are carried out on other molecules and in other circuits. Beyond instructing target selection, members of the teneurin and latrophilin families have been shown to have roles in synapse formation in later stages of development within these same regions.[50–52]

The second mechanism is the repeated use of a molecular module—Ten3–Ten3-mediated attraction and Ten3–Lphn2-mediated mutual repulsions—across multiple nodes of the same circuit and potentially many

circuits across the brain. We have used systematic conditional knockouts to demonstrate conclusively the repeated use of this molecular module in instructing hard-wired connections in the extended hippocampal network. Our companion manuscript reported the broad deployment of inverse expression of Ten3 and Lphn2 across many circuits in the mouse brain and the spinal cord.[40,53] In all these cases, Ten3–Lphn2 inverse expression patterns lay out a topographic map in the developing brain prior to the presence of functional connections. These studies also highlight the need for exquisite spatiotemporal control of their expression, and the collaboration with other guidance molecules, such that Ten3$^+$/Lphn2$^+$ neurons from one circuit do not encounter Ten3$^+$/Lphn2$^+$ neurons from another circuit to prevent unintended cross interactions.

An outstanding question for future research is how the inverse expression patterns of Ten3 and Lphn2 are established during development. Are there shared transcriptional regulatory mechanisms across different brain regions, or do these mechanisms differ region by region? Additionally, other connections within the extended hippocampal network are topographic with inverse expression, including CA1→entorhinal cortex, subiculum→entorhinal cortex, subiculum →anteroventral thalamus, and mMN→anteroventral thalamus (Figure 1A$_3$),[30,34,36,54–57] making it an ideal place to test target selection mechanisms that underlie reciprocal and recurrent connections. Finally, although we know that Lphn2 in lateral hippocampal network is repelled by Ten3 in medial hippocampal network, it has no homophilic binding properties.[11,47] Are there yet-to-be-identified heterophilic attractive partners for Lphn2$^+$ neurons, which will make the Ten3–Lphn2 molecular module more symmetrical?

REFERENCES

1. Sperry RW. Chemoaffinity in the orderly growth of nerve fiber patterns and connections*. *Proc Natl Acad Sci*. 1963;50(4):703-710. doi:10.1073/pnas.50.4.703
2. Sanes JR, Zipursky SL. Synaptic Specificity, Recognition Molecules, and Assembly of Neural Circuits. *Cell*. 2020;181(3):536-556. doi:10.1016/j.cell.2020.04.008
3. Kolodkin AL, Tessier-Lavigne M. Mechanisms and Molecules of Neuronal Wiring: A Primer. *Cold Spring Harb Perspect Biol*. 2011;3(6):a001727. doi:10.1101/cshperspect.a001727
4. Walter J, Kern-Veits B, Huf J, Stolze B, Bonhoeffer F. Recognition of position-specific properties of tectal cell membranes by retinal axons in vitro. *Development*. 1987;101(4):685-696.
5. Cheng HJ, Nakamoto M, Bergemann AD, Flanagan JG. Complementary gradients in expression and binding of ELF-1 and Mek4 in development of the topographic retinotectal projection map. *Cell*. 1995;82(3):371-381. doi:10.1016/0092-8674(95)90426-3
6. Drescher U, Kremoser C, Handwerker C, Löschinger J, Noda M, Bonhoeffer F. In vitro guidance of retinal ganglion cell axons by RAGS, a 25 kDa tectal protein related to ligands for Eph receptor tyrosine kinases. *Cell*. 1995;82(3):359-370. doi:10.1016/0092-8674(95)90425-5
7. Inaki M, Yoshikawa S, Thomas JB, Aburatani H, Nose A. Wnt4 Is a Local Repulsive Cue that Determines Synaptic Target Specificity. *Curr Biol*. 2007;17(18):1574-1579. doi:10.1016/j.cub.2007.08.013
8. Hong W, Mosca TJ, Luo L. Teneurins instruct synaptic partner matching in an olfactory map. *Nature*. 2012;484(7393):201-207. doi:10.1038/nature10926
9. Mosca TJ, Hong W, Dani VS, Favaloro V, Luo L. Trans-synaptic Teneurin signalling in neuromuscular synapse organization and target choice. *Nature*. 2012;484(7393):237-241. doi:10.1038/nature10923
10. Berns DS, DeNardo LA, Pederick DT, Luo L. Teneurin-3 controls topographic circuit assembly in the hippocampus. *Nature*. 2018;554(7692):328-333. doi:10.1038/nature25463
11. Pederick DT, Lui JH, Gingrich EC, et al. Reciprocal repulsions instruct the precise assembly of parallel hippocampal networks. *Science*. 2021;372(6546):1068-1073. doi:10.1126/science.abg1774
12. Li Z, Lyu C, Xu C, et al. Repulsive interactions instruct synaptic partner matching in an olfactory circuit. Published online July 19, 2025:2025.03.01.640985. doi:10.1101/2025.03.01.640985
13. Lyu C, Li Z, Xu C, et al. Dimensionality reduction simplifies synaptic partner matching in an olfactory circuit. *Science*. 2025;388(6746):538-544. doi:10.1126/science.ads7633
14. Azevedo FAC, Carvalho LRB, Grinberg LT, et al. Equal numbers of neuronal and nonneuronal cells make the human brain an isometrically scaled-up primate brain. *J Comp Neurol*. 2009;513(5):532-541. doi:10.1002/cne.21974
15. Andrade-Moraes CH, Oliveira-Pinto AV, Castro-Fonseca E, et al. Cell number changes in Alzheimer's disease relate to dementia, not to plaques and tangles. *Brain J Neurol*. 2013;136(Pt 12):3738-3752. doi:10.1093/brain/awt273
16. Goriely A. Eighty-six billion and counting: do we know the number of neurons in the human brain? *Brain*. 2025;148(3):689-691. doi:10.1093/brain/awae390
17. Bausch-Fluck D, Goldmann U, Müller S, et al. The in silico human surfaceome. *Proc Natl Acad Sci*. 2018;115(46):E10988-E10997. doi:10.1073/pnas.1808790115
18. Luo L. *Principles of Neurobiology*. 2nd ed. CRC Press; 2021.
19. Cang J, Feldheim DA. Developmental Mechanisms of Topographic Map Formation and Alignment. *Annu Rev Neurosci*. 2013;36(1):51-77. doi:10.1146/annurev-neuro-062012-170341
20. Nakamoto M, Cheng HJ, Friedman GC, et al. Topographically Specific Effects of ELF-1 on Retinal Axon Guidance In Vitro and Retinal Axon Mapping In Vivo. *Cell*. 1996;86(5):755-766. doi:10.1016/S0092-8674(00)80150-6
21. Frisén J, Yates PA, McLaughlin T, Friedman GC, O'Leary DDM, Barbacid M. Ephrin-A5 (AL-1/RAGS) Is Essential for Proper Retinal Axon Guidance and Topographic Mapping in the Mammalian Visual System. *Neuron*. 1998;20(2):235-243. doi:10.1016/S0896-6273(00)80452-3

22. Brown A, Yates PA, Burrola P, et al. Topographic Mapping from the Retina to the Midbrain Is Controlled by Relative but Not Absolute Levels of EphA Receptor Signaling. *Cell*. 2000;102(1):77-88. doi:10.1016/S0092-8674(00)00012-X
23. Feldheim DA, Kim YI, Bergemann AD, Frisén J, Barbacid M, Flanagan JG. Genetic Analysis of Ephrin-A2 and Ephrin-A5 Shows Their Requirement in Multiple Aspects of Retinocollicular Mapping. *Neuron*. 2000;25(3):563-574. doi:10.1016/S0896-6273(00)81060-0
24. Rashid T, Upton AL, Blentic A, et al. Opposing Gradients of Ephrin-As and EphA7 in the Superior Colliculus Are Essential for Topographic Mapping in the Mammalian Visual System. *Neuron*. 2005;47(1):57-69. doi:10.1016/j.neuron.2005.05.030
25. Egea J, Klein R. Bidirectional Eph–ephrin signaling during axon guidance. *Trends Cell Biol*. 2007;17(5):230-238. doi:10.1016/j.tcb.2007.03.004
26. Triplett JW, Owens MT, Yamada J, et al. Retinal input instructs alignment of visual topographic maps. *Cell*. 2009;139(1):175-185. doi:10.1016/j.cell.2009.08.028
27. Suetterlin P, Drescher U. Target-Independent EphrinA/EphA-Mediated Axon-Axon Repulsion as a Novel Element in Retinocollicular Mapping. *Neuron*. 2014;84(4):740-752. doi:10.1016/j.neuron.2014.09.023
28. Igarashi KM, Ito HT, Moser EI, Moser MB. Functional diversity along the transverse axis of hippocampal area CA1. *FEBS Lett*. 2014;588(15):2470-2476. doi:10.1016/j.febslet.2014.06.004
29. Cembrowski MS, Phillips MG, DiLisio SF, et al. Dissociable Structural and Functional Hippocampal Outputs via Distinct Subiculum Cell Classes. *Cell*. 2018;173(5):1280-1292.e18. doi:10.1016/j.cell.2018.03.031
30. Tamamaki N, Nojyo Y. Preservation of topography in the connections between the subiculum, field CA1, and the entorhinal cortex in rats. *J Comp Neurol*. 1995;353(3):379-390. doi:10.1002/cne.903530306
31. Allen GV, Hopkins DA. Mamillary body in the rat: topography and synaptology of projections from the subicular complex, prefrontal cortex, and midbrain tegmentum. *J Comp Neurol*. 1989;286(3):311-336. doi:10.1002/cne.902860303
32. Shibata H. Descending projections to the mammillary nuclei in the rat, as studied by retrograde and anterograde transport of wheat germ agglutinin-horseradish peroxidase. *J Comp Neurol*. 1989;285(4):436-452. doi:10.1002/cne.902850403
33. Kishi T, Tsumori T, Ono K, Yokota S, Ishino H, Yasui Y. Topographical organization of projections from the subiculum to the hypothalamus in the rat. *J Comp Neurol*. 2000;419(2):205-222. doi:10.1002/(SICI)1096-9861(20000403)419:2<205::AID-CNE5>3.0.CO;2-0
34. Naber PA, Lopes da Silva FH, Witter MP. Reciprocal connections between the entorhinal cortex and hippocampal fields CA1 and the subiculum are in register with the projections from CA1 to the subiculum. *Hippocampus*. 2001;11(2):99-104. doi:10.1002/hipo.1028
35. van Strien NM, Cappaert NLM, Witter MP. The anatomy of memory: an interactive overview of the parahippocampal–hippocampal network. *Nat Rev Neurosci*. 2009;10(4):272-282. doi:10.1038/nrn2614
36. Wright NF, Erichsen JT, Vann SD, O'Mara SM, Aggleton JP. Parallel but separate inputs from limbic cortices to the mammillary bodies and anterior thalamic nuclei in the rat. *J Comp Neurol*. 2010;518(12):2334-2354. doi:10.1002/cne.22336
37. Pederick DT, Perry-Hauser NA, Meng H, He Z, Javitch JA, Luo L. Context-dependent requirement of G protein coupling for Latrophilin-2 in target selection of hippocampal axons. *eLife*. 2023;12:e83529. doi:10.7554/eLife.83529
38. Donohue JD, Amidon RF, Murphy TR, et al. Parahippocampal latrophilin-2 (ADGRL2) expression controls topographical presubiculum to entorhinal cortex circuit connectivity. *Cell Rep*. 2021;37(8):110031. doi:10.1016/j.celrep.2021.110031
39. Liakath-Ali K, Refaee R, Südhof TC. Cartography of teneurin and latrophilin expression reveals spatiotemporal axis heterogeneity in the mouse hippocampus during development. *PLOS Biol*. 2024;22(5):e3002599. doi:10.1371/journal.pbio.3002599
40. Chon Ur, Pederick DT, Song JH, Zhang Y, Rana I, Luo L. Inverse expression of Ten3 and Lphn2 across the developing mouse brain reveals a global strategy for circuit assembly. Published online 2025.

41. Wang F, Flanagan J, Su N, et al. RNAscope: A Novel in Situ RNA Analysis Platform for Formalin-Fixed, Paraffin-Embedded Tissues. *J Mol Diagn*. 2012;14(1):22-29. doi:10.1016/j.jmoldx.2011.08.002
42. The MouseLight Project. https://ml-neuronbrowser.janelia.org/
43. Digital Brain - Projectome Atlas. https://mouse.digital-brain.cn/projectome
44. Qiu S, Hu Y, Huang Y, et al. Whole-brain spatial organization of hippocampal single-neuron projectomes. *Science*. 2024;383(6682):eadj9198. doi:10.1126/science.adj9198
45. Winnubst J, Bas E, Ferreira TA, et al. Reconstruction of 1,000 Projection Neurons Reveals New Cell Types and Organization of Long-Range Connectivity in the Mouse Brain. *Cell*. 2019;179(1):268-281.e13. doi:10.1016/j.cell.2019.07.042
46. Economo MN, Clack NG, Lavis LD, et al. A platform for brain-wide imaging and reconstruction of individual neurons. Ginty DD, ed. *eLife*. 2016;5:e10566. doi:10.7554/eLife.10566
47. Boucard AA, Maxeiner S, Südhof TC. Latrophilins Function as Heterophilic Cell-adhesion Molecules by Binding to Teneurins: REGULATION BY ALTERNATIVE SPLICING*. *J Biol Chem*. 2014;289(1):387-402. doi:10.1074/jbc.M113.504779
48. Imai T, Yamazaki T, Kobayakawa R, et al. Pre-target axon sorting establishes the neural map topography. *Science*. 2009;325(5940):585-590. doi:10.1126/science.1173596
49. Luo L. Architectures of neuronal circuits. *Science*. 2021;373(6559):eabg7285. doi:10.1126/science.abg7285
50. Anderson GR, Maxeiner S, Sando R, Tsetsenis T, Malenka RC, Südhof TC. Postsynaptic adhesion GPCR latrophilin-2 mediates target recognition in entorhinal-hippocampal synapse assembly. *J Cell Biol*. 2017;216(11):3831-3846. doi:10.1083/jcb.201703042
51. Sando R, Jiang X, Südhof TC. Latrophilin GPCRs direct synapse specificity by coincident binding of FLRTs and teneurins. *Science*. 2019;363(6429):eaav7969. doi:10.1126/science.aav7969
52. Sando R, Südhof TC. Latrophilin GPCR signaling mediates synapse formation. Davis GW, Westbrook GL, Davis GW, eds. *eLife*. 2021;10:e65717. doi:10.7554/eLife.65717
53. Kevin T. Sangster, Xinying Zhang, Daniel del Toro, et al. Teneurin-3 and Latrophilin-2 are required for the formation of a somatotopic map and somatosensory topognosis. Published online 2025.
54. Wright NF, Vann SD, Erichsen JT, O'Mara SM, Aggleton JP. Segregation of parallel inputs to the anteromedial and anteroventral thalamic nuclei of the rat. *J Comp Neurol*. 2013;521(13):2966-2986. doi:10.1002/cne.23325
55. Seki M, Zyo K. Anterior thalamic afferents from the mamillary body and the limbic cortex in the rat. *J Comp Neurol*. 1984;229(2):242-256. doi:10.1002/cne.902290209
56. Hayakawa T, Zyo K. Retrograde double-labeling study of the marnmillothalamic and the mammillotegmental projections in the rat. *J Comp Neurol*. 1989;284(1):1-11. doi:10.1002/cne.902840102
57. Shibata H. Topographic organization of subcortical projections to the anterior thalamic nuclei in the rat. *J Comp Neurol*. 1992;323(1):117-127. doi:10.1002/cne.903230110

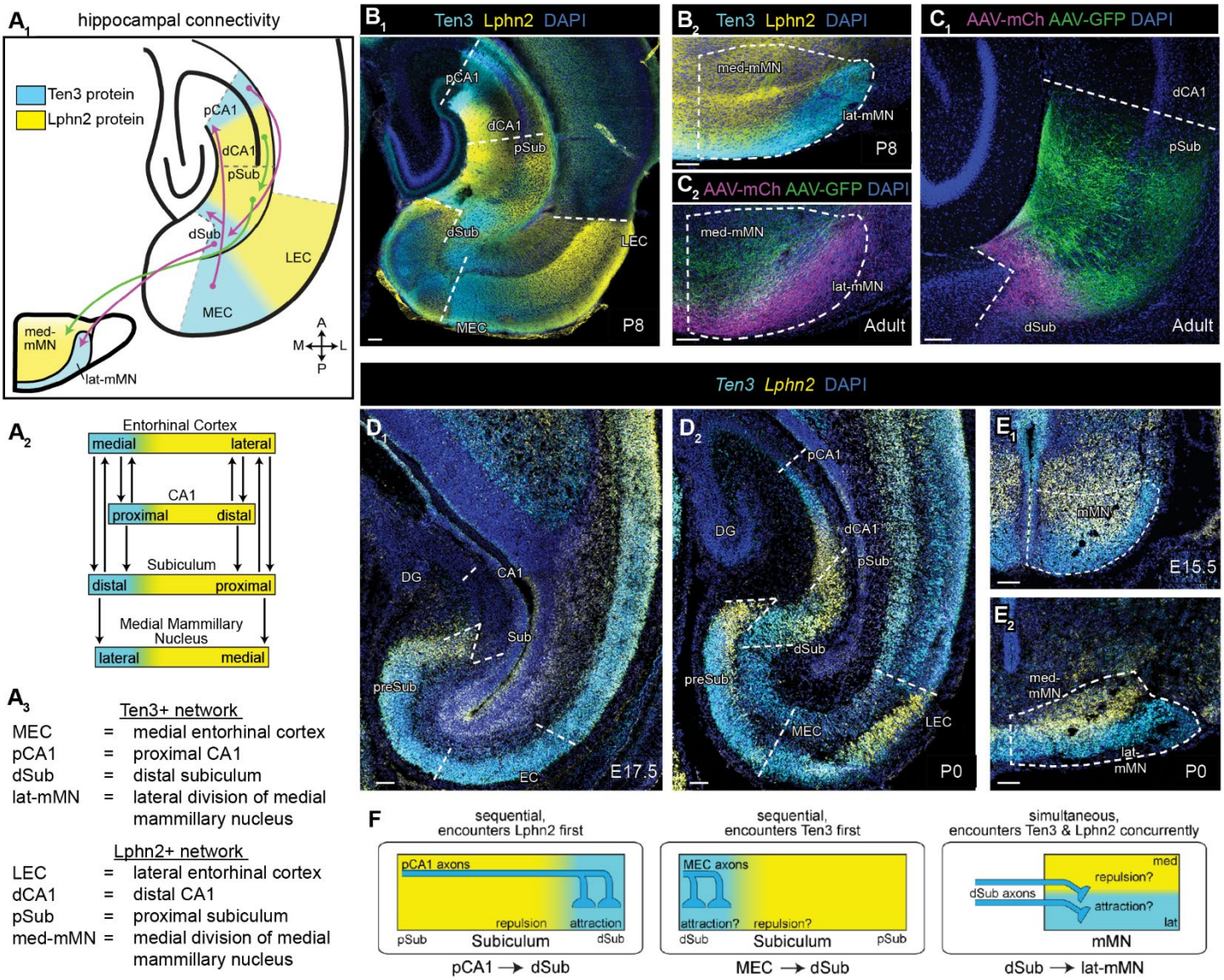

Figure 1. Inverse Ten3 and Lphn2 expression patterns match the topography of the extended hippocampal network during development.

(A) Summary of topographic connectivity addressed in this study, overlaid on P8 Ten3 and Lphn2 protein expression (A_1). All connectivity between four different nodes of the medial and lateral hippocampal network (A_2), with relevant anatomical abbreviations (A_3).

(B) Inverse protein expression of Ten3 and Lphn2 in hippocampus and entorhinal cortex (B_1) and medial mammillary nucleus (mMN) of the hypothalamus (B_2) of P8 *Ten3*$^{HA/HA}$;*Lphn2*$^{mV/mV}$ mouse.

(C) Dual anterograde tracer injections into neighboring sites in distal subiculum (dSub) and proximal subiculum (pSub; C_1) result in topographic projections to neighboring sites in lateral (lat-mMN) and medial (med-mMN) mMN, respectively (C_2).

(D) mRNA expression of *Ten3* (cyan) and *Lphn2* (yellow) at E17.5 (D_1) and P0 (D_2) in hippocampus and entorhinal cortex. At E17.5, only *Ten3* mRNA is detectable in EC. By P0, CA1, Sub, and EC all have inverse mRNA expression of *Ten3* and *Lphn2*.

(E) mRNA expression of *Ten3* (cyan) and *Lphn2* (yellow) at E15.5 (E_1) and P0 (E_2) in mMN.

(F) Summary of three different axon entry routes with respect to Ten3 and Lphn2 expression subfields in target. Scale bars, 100 μm. See Figure S1 for additional data.

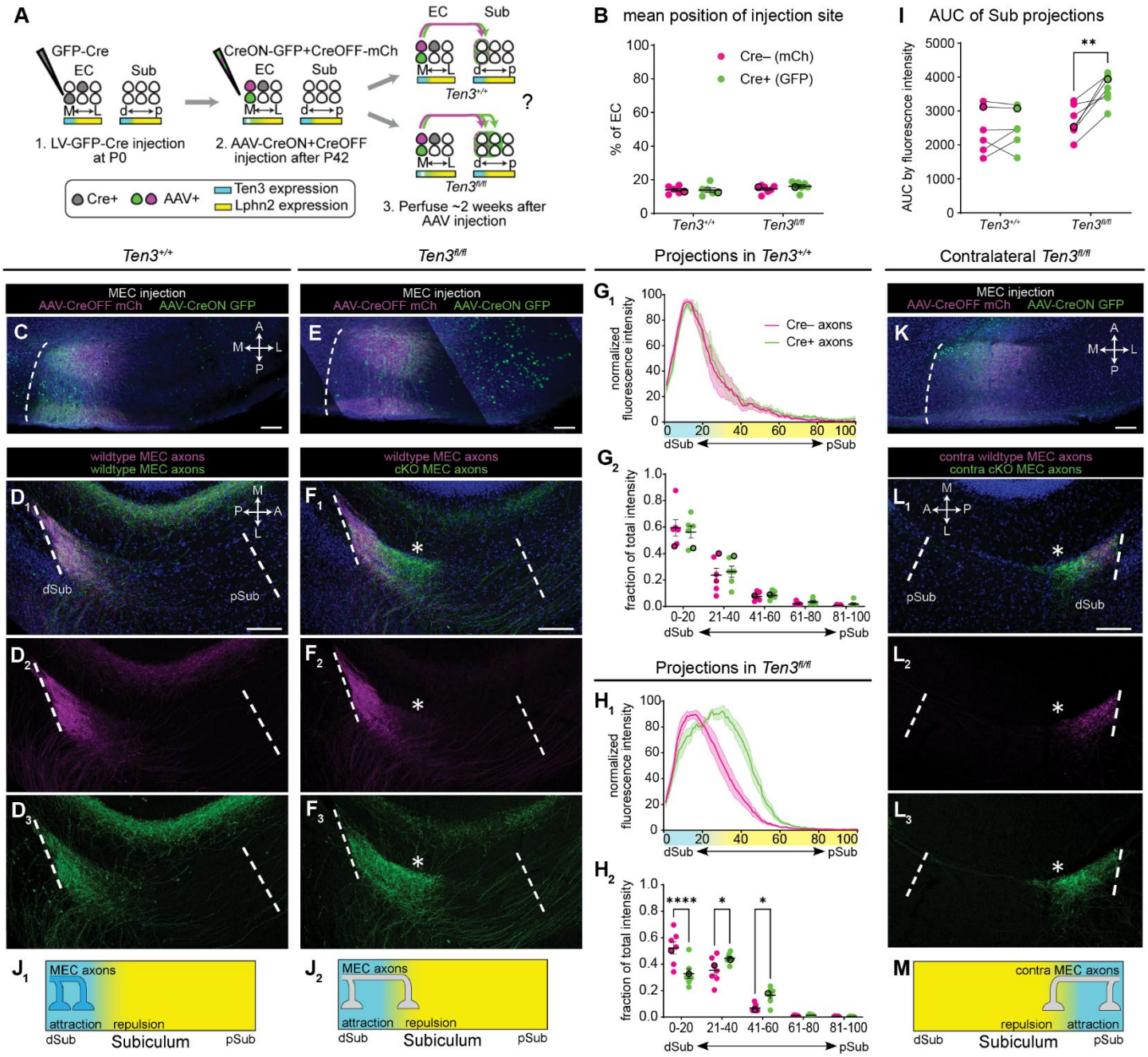

Figure 2. Ten3 is required in medial entorhinal cortex axons for their precise targeting to distal subiculum

(A) Injection strategy and possible results for tracing MEC axons into subiculum of control (top right) and *Ten3*$^{fl/fl}$ mice (bottom right).

(B) Mean position of injection sites along the medial→lateral axis of entorhinal cortex (EC) show no differences between *Ten3*$^{+/+}$ controls (n = 6 mice) and *Ten3*$^{fl/fl}$ mice (n = 7 mice). Black outline indicates representative animals shown in C, E. Mean ± SEM. Unpaired t-tests corrected for multiple comparisons (Holm-Šídák with Welch correction). No significant differences.

(C) Representative image of the *AAV-CreON/CreOFF* injection site of *Ten3*$^{+/+}$ controls show both viruses restricted to the most medial region of entorhinal cortex. Injection corresponds to animal in D. Scale bar, 100 µm.

(D) Representative images of projection of Cre^{-} axons (magenta) and Cre^{+} axons (green) into molecular layer of subiculum in *Ten3*$^{+/+}$ controls. The three images are from the same confocal section showing merge (D_1), magenta only (D_2), or green only (D_3) channels. Scale bar, 100 µm.

(E, F) Same as C, D but for *Ten3*$^{fl/fl}$ mice. *Ten3* cKO axons in *Ten3*$^{fl/fl}$ mice spread beyond the Cre^{-} control axons toward pSub (asterisk in F, in identical position across three images).
(G_1) Normalized fluorescence intensity traces of the Cre^{-} (magenta) and Cre^{+} (green) projections along the distal–proximal axis of subiculum in *Ten3*$^{+/+}$ controls (n = 6 mice). Ten3 (cyan) and Lphn2 (yellow) expression is represented along the x-axis. Mean (dark line) ± SEM (shaded area).
(G_2) Fraction of total projection intensity (same data as G_1) in 20% bins of subiculum axis of the Cre^{-} (magenta) and Cre^{+} (green) projections along the distal–proximal axis of subiculum in *Ten3*$^{+/+}$ controls (n = 6 mice). Open circles indicate representative animal shown in D. Mean ± SEM. Two-way ANOVA corrected for multiple comparisons (Šídák correction), no significant differences.
(H) Same as G but for *Ten3*$^{fl/fl}$ (n = 7) mice. **** $p < 0.0001$, * $p < 0.05$.
(I) Area under the curve of averaged subiculum projections for *Ten3*$^{+/+}$ controls (n = 6 mice) and *Ten3*$^{fl/fl}$ mice (n = 7 mice). Lines are drawn between Cre^{-} (magenta) and Cre^{+} (green) projections within the same animal. Open circles indicate representative animals shown in D, F. Unpaired t-tests corrected for multiple comparisons (Holm-Šídák with Welch correction), ** $p < 0.01$.
(J) Schematic summary of target selection of MEC axons in subiculum in control (J_1) and *Ten3*^{MEC}-cKO (J_2) based on results in C–I.
(K, L) Same as E, F, but for projections into contralateral subiculum. Contralateral Cre^{+}, *Ten3* cKO axons in *Ten3*$^{fl/fl}$ mice spread beyond the contralateral Cre^{-} control axons toward pSub (asterisk, in identical position across three images).
(M) Schematic summary of target selection of MEC axons in contralateral subiculum in *Ten3*^{MEC}-cKO mice.
See Figure S2 for additional data.

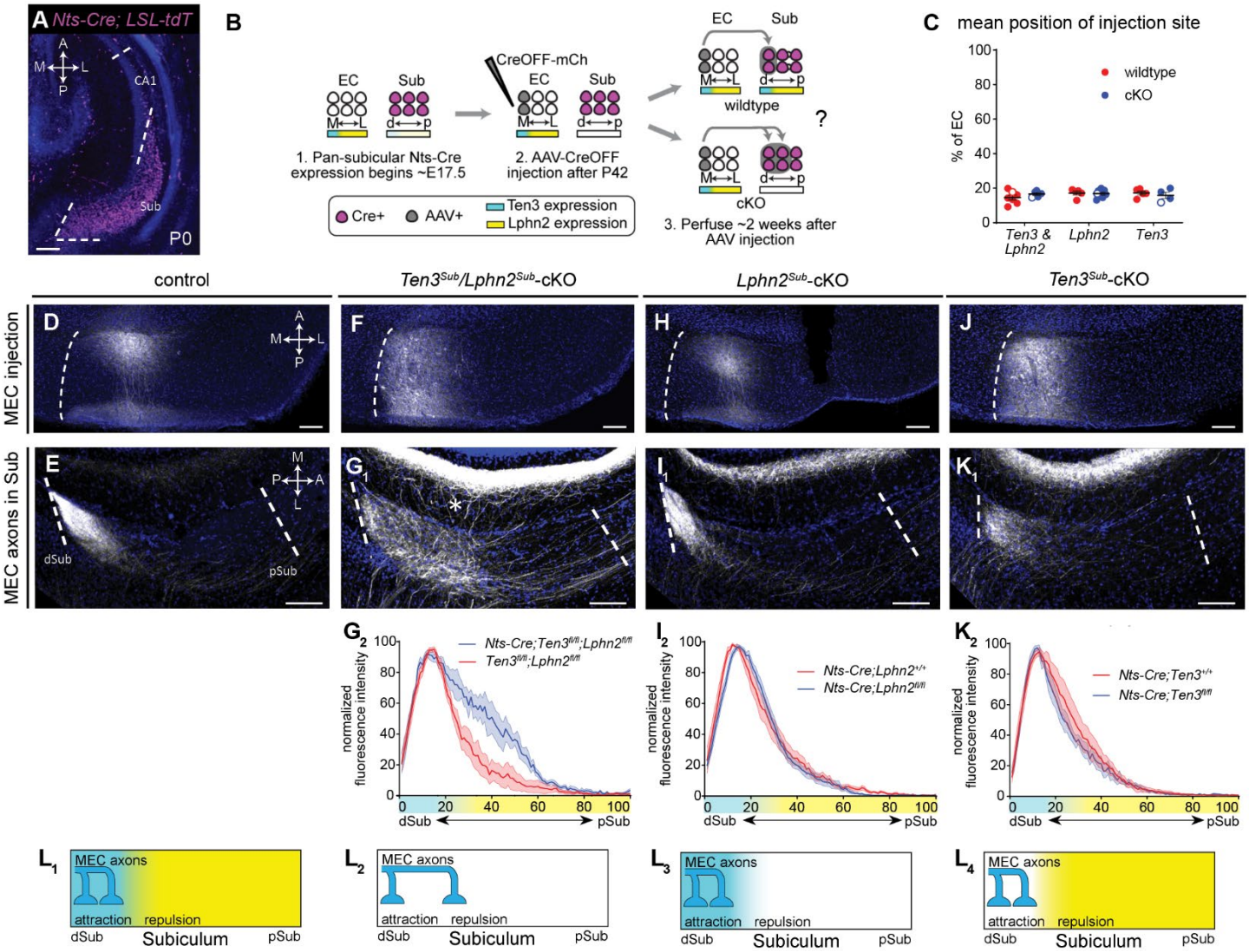

Figure 3. Ten3 and Lphn2 in subiculum cooperate to instruct the precise targeting of medial entorhinal cortex axons

(A) *Nts-Cre* is densely expressed in subiculum at P0, as assessed by a nuclear tdTomato reporter. Scale bar, 150 µm.

(B) Injection strategy and possible results for tracing MEC axons into subiculum of control (top right) and *Nts-Cre;Ten3$^{fl/fl}$;Lphn2$^{fl/fl}$* double cKO mice (bottom right).

(C) Mean position of injection sites along the medial→lateral axis of entorhinal cortex (EC) show no differences between *Ten3^{Sub}/Lphn2^{Sub}*-cKO (n = 5 mice), *Lphn2^{Sub}*-cKO (n = 7 mice), *Ten3^{Sub}*-cKO (n = 4 mice), and their respective littermate controls (n=5, 5, 4, respectively). Open circles indicate representative animals shown in D, F, H, J. Mean ± SEM. Unpaired t-test with Welch correction, no significant differences.

(D) Representative image of the *AAV-CreOFF* injection site of *Ten3$^{fl/fl}$;Lphn2$^{fl/fl}$* controls shows virus is restricted to the most medial region of entorhinal cortex. Injection corresponds to animal in E. Scale bar, 100 µm.

(E) Representative image of projection into molecular layer of subiculum for *Ten3$^{fl/fl}$;Lphn2$^{fl/fl}$* (control). Scale bar, 100 µm.

(F, H, J) Same as D, but for genotypes indicated above.

(G_1, I_1, K_1) Same as E, but for genotypes indicated above. MEC axons in *Ten3^{Sub}/Lphn2^{Sub}*-cKO mice spread proximally beyond dSub (asterisk in G_1).

(G_2, I_2, K_2) Normalized fluorescence intensity traces in genotypes as indicated. Mean (dark line) ± SEM (shaded area). n = 7, 5 for control and *Ten3^{Sub}/Lphn2^{Sub}*-cKO mice, respectively (G_2); n = 5, 7 for control and *Lphn2^{Sub}*-

cKO mice, respectively (I_2); n = 5, 4 for control and *Ten3*^{Sub}-cKO mice, respectively (K_2). Ten3 (cyan) and Lphn2 (yellow) expression is represented along the x-axis. Mean (dark line) ± SEM (shaded area).
(L) Schematic summary of target selection of MEC axons in subiculum when *Ten3* (L_4), *Lphn2* (L_3), or both (L_2) were conditionally knocked out in subiculum target.
See Figure S3–S4 for additional data. See Table S1 for detailed genotypes.

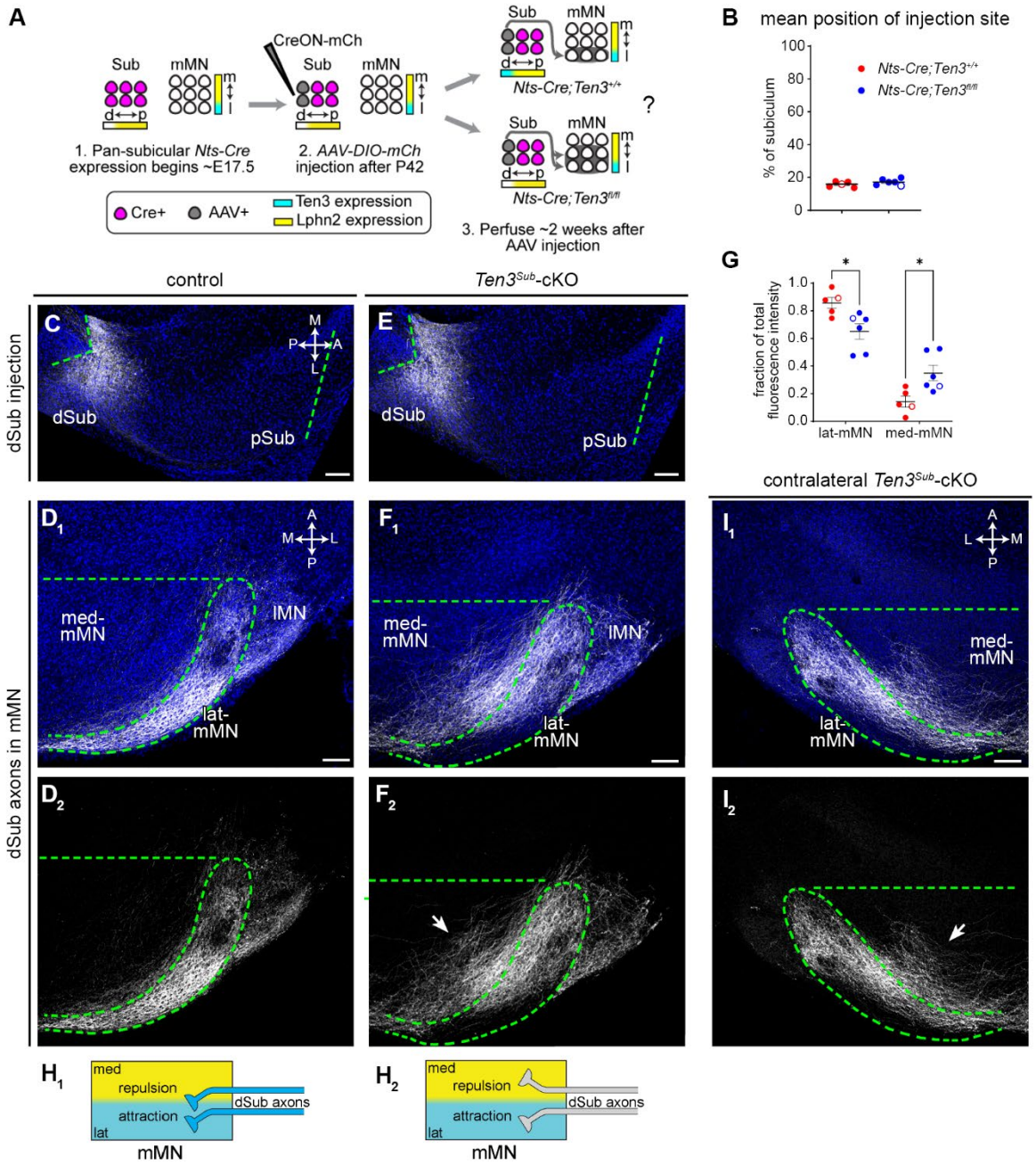

Figure 4. Ten3 is required in subiculum for dSub axons to precisely targeting to lateral mMN.
(A) Injection strategy and possible results for tracing dSub axons into medial mammillary nucleus (mMN) of *Nts-Cre;Ten3*$^{+/+}$ control (top right) and *Nts-Cre;Ten3*$^{fl/fl}$ mice (bottom right).
(B) Mean positions of injection sites along the distal→proximal axis of subiculum show no differences between *Nts-Cre;Ten3*$^{+/+}$ controls (n = 5 mice) and *Ten3*^{Sub}-cKO (n = 6 mice). Open circles indicate representative animals shown in C, E. Mean ± SEM. Unpaired t-test with Welch correction, no significant differences.
(C) Representative image of the *AAV-mCh* (gray) injection site of *Nts-Cre;Ten3*$^{+/+}$ controls show the virus is restricted to the most distal region of subiculum. Injection corresponds to animal in D. Scale bar, 100 µm.
(D) Representative images of projection of dSub axons (gray) into mMN of *Nts-Cre;Ten3*$^{+/+}$ controls (D_1). Bottom panel shows axons without DAPI counterstain (D_2). Labeling in the lateral mammillary nucleus (lMN) are unrelated axons from pre-subiculum. Scale bar, 100 µm.
(E, F) Same as C, D, but for *Ten3*^{Sub}-cKO mice. *Ten3* cKO axons spread outside of the lat-mMN (arrow).

(G) Fraction of total projection intensity in lat-mMN (left) versus med-mMN (right) of the dSub axons in *Nts-Cre;Ten3*$^{+/+}$ controls (red) and *Ten3*^{Sub}-cKO (blue). Open circles indicate representative animals shown in D, F. Mean ± SEM. Unpaired t-tests corrected for multiple comparisons (Holm-Šídák with Welch correction), * $p < 0.05$.
(H) Schematic summary of target selection of dSub axons in mMN of control (H_1) and *Ten3*^{Sub}-cKO (H_2) mice based on results in C–G.
(I) Same as F, but for projections into contralateral mMN. Contralateral *Ten3* cKO axons spread outside of the lat-mMN (arrow).
Anatomical borders were drawn based on DAPI counterstain.
See Figure S3, S5, and S7 for additional data. See Table S1 for detailed genotypes.

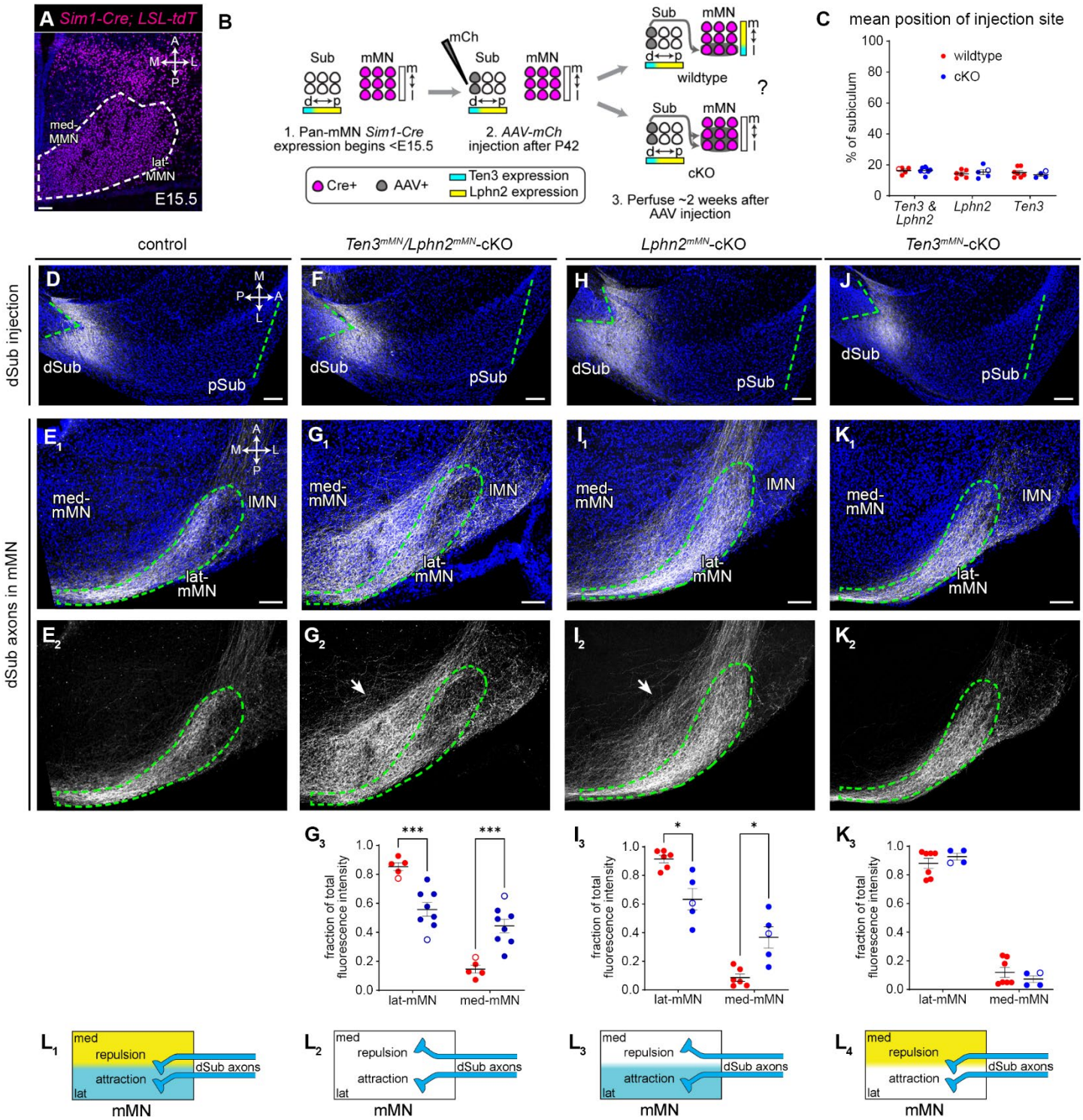

Figure 5. Lphn2 is required in mMN for the precise targeting of dSub axons to lat-mMN

(A) *Sim1-Cre* is densely expressed in mMN by E15.5, as assessed by a nuclear tdTomato reporter. Scale bar, 50 µm.

(B) Injection strategy and possible results for tracing dSub axons into medial mammillary nucleus (mMN) of controls (top right) and *Sim1-Cre;Ten3*$^{fl/fl}$*;Lphn2*$^{fl/fl}$ cKO mice (bottom right).

(C) Mean positions of injection sites along the distal→proximal axis of subiculum show no differences between *Ten3*^{mMN}*/Lphn2*^{mMN}-cKO (left; n=8), *Lphn2*^{mMN}-cKO (middle; n=5), *and Ten3*^{mMN}-cKO (right; n=4), and their respective littermate controls (n=5, 6, 7, respectively. Open circles indicate representative animals shown in D,

F, H, J. Mean ± SEM. Unpaired t-tests corrected for multiple comparisons (Holm-Šídák with Welch correction), no significant differences.
(D) Representative image of the *AAV-mCh* (gray) injection site of *Ten3*$^{fl/fl}$*;Lphn2*$^{fl/fl}$ controls show the virus is restricted to the most distal region of subiculum. Injection corresponds to animal in E. Scale bar, 100 µm.
(E) Representative images of projection into mMN of *Ten3*$^{fl/fl}$*;Lphn2*$^{fl/fl}$ control mice (E_1). Bottom panel shows axons without DAPI counterstain (E_2). Labeling in lMN are unrelated axons from pre-subiculum. Scale bar, 100 µm.
(F, H, J) Same as D, but for genotypes indicated above.
($G_{1,2}$, $I_{1,2}$, $K_{1,2}$) Same as E, but for genotypes indicated above. dSub axons in *Ten3*^{mMN}*/Lphn2*^{mMN}-cKO (G) and *Lphn2*^{mMN}-cKO (I) mice spread medially outside of lat-mMN (arrows in G_2, I_2).
(G_3, I_3, K_3) Fraction of total projection intensity in lat-mMN (left) versus med-mMN (right) of the dSub axons in mMN of genotypes as indicated. n = 5, 8 for control and *Ten3*^{mMN}*/Lphn2*^{mMN}-cKO mice, respectively (G_2); n = 6, 5 for control and *Lphn2*^{mMN}-cKO mice, respectively (I_2); n = 7, 4 for control and *Ten3*^{mMN}-cKO mice, respectively (K_2). Open circles indicate representative animals shown in E, G, I, K. Mean ± SEM. Unpaired t-tests corrected for multiple comparisons (Holm-Šídák with Welch correction), * $p < 0.05$, *** $p < 0.001$.
(L) Schematic summary of target selection of dSub axons in mMN when *Ten3* (L_4), *Lphn2* (L_3), or both (L_2) were conditionally knocked out in mMN.
Anatomical borders were drawn based on DAPI counterstain
See Figure S3 and S6 for additional data. See Table S1 for detailed genotypes.

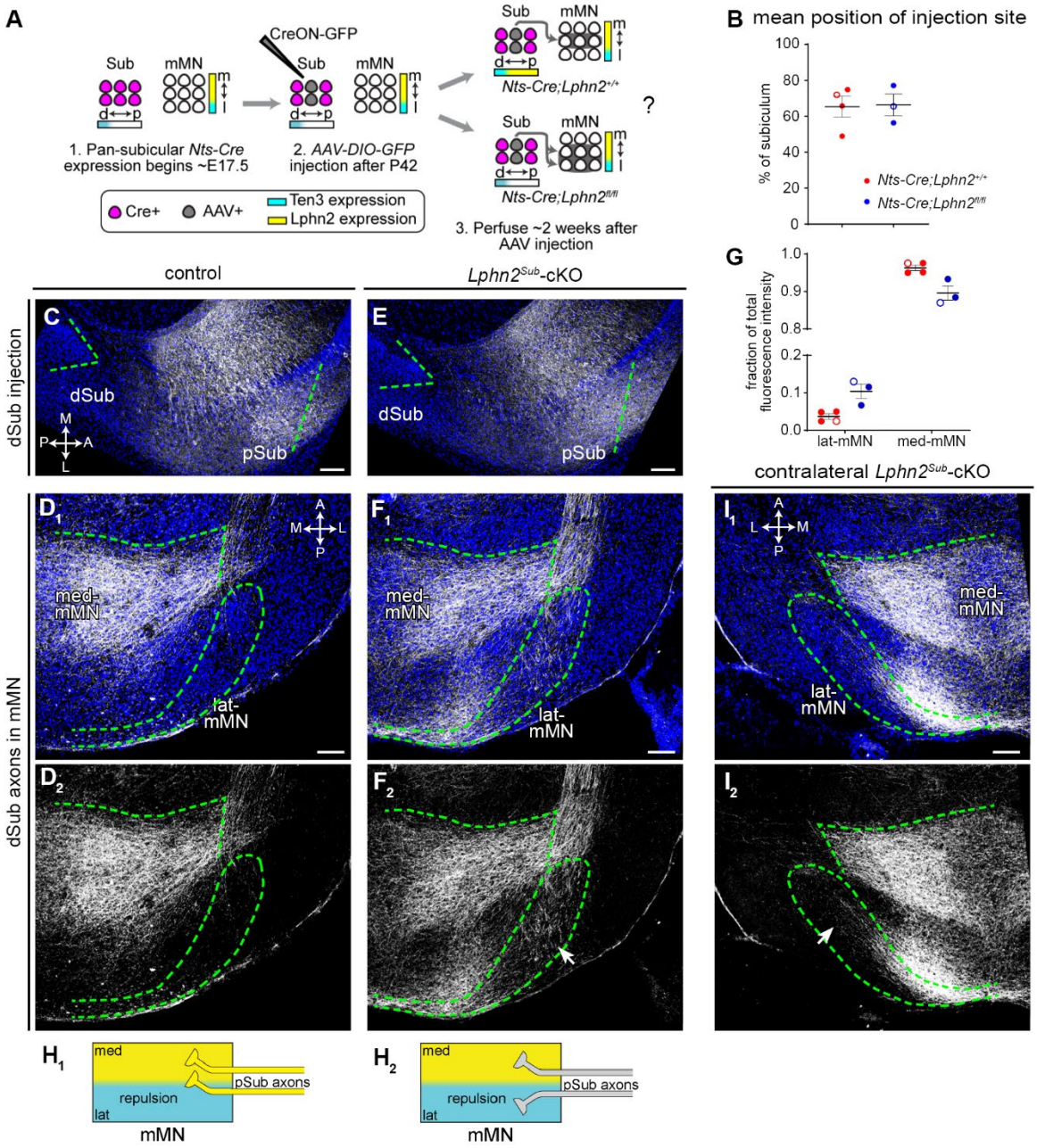

Figure 6. Lphn2 is required in subiculum for pSub axons to precisely target to medial mMN.
(A) Injection strategy and possible results for tracing proximal subiculum (pSub) axons into mMN of control (top right) and *Nts-Cre;Lphn2*$^{fl/fl}$ mice (bottom right).
(B) Mean positions of injection sites along the distal→proximal axis of subiculum show no differences between *Nts-Cre;Lphn2*$^{+/+}$ controls (n = 4 mice) and *Lphn2*^{Sub}-cKO mice (n = 3 mice). Open circles indicate representative animals shown in C, E. Mean ± SEM. Unpaired t-test with Welch correction, no significant differences.
(C) Representative image of the *AAV-mCh* (gray) injection site of *Nts-Cre;Lphn2*$^{+/+}$ controls show the virus in pSub and pSub and does not reach dSub. Injection corresponds to animal in D. Scale bar, 100 µm.
(D) Representative images of projection of pSub axons (gray) into mMN of *Nts-Cre;Lphn2*$^{+/+}$ controls (D_1). Bottom panel shows axons without DAPI counterstain (D_2). Scale bar, 100 µm.
(E, F) Same as C, D, but for *Lphn2*^{Sub}-cKO mice. *Lphn2* cKO axons spread outside of med-mMN and into lat-mMN (arrow in F_2).

(G) Fraction of total projection intensity of pSub axons in lat-mMN (left) versus med-mMN (right) of the pSub axons *Nts-Cre;Lphn2*$^{+/+}$ controls (red) and *Lphn2*^{Sub}-cKO (blue). Open circles indicate representative animals shown in D, F. Mean ± SEM.
(H) Schematic summary of target selection of pSub axons in mMN of control (H_1) and *Lphn2*^{Sub}-cKO (H_2) mice based on results in C–G.
(I) Same as F, but for projections into contralateral mMN. Contralateral *Lphn2* cKO axons spread outside of med-mMN and into lat-mMN (arrow in I_2).
Anatomical borders were drawn based on DAPI counterstain.
See Figure S3 and S7 for additional data. See Table S1 for detailed genotypes.

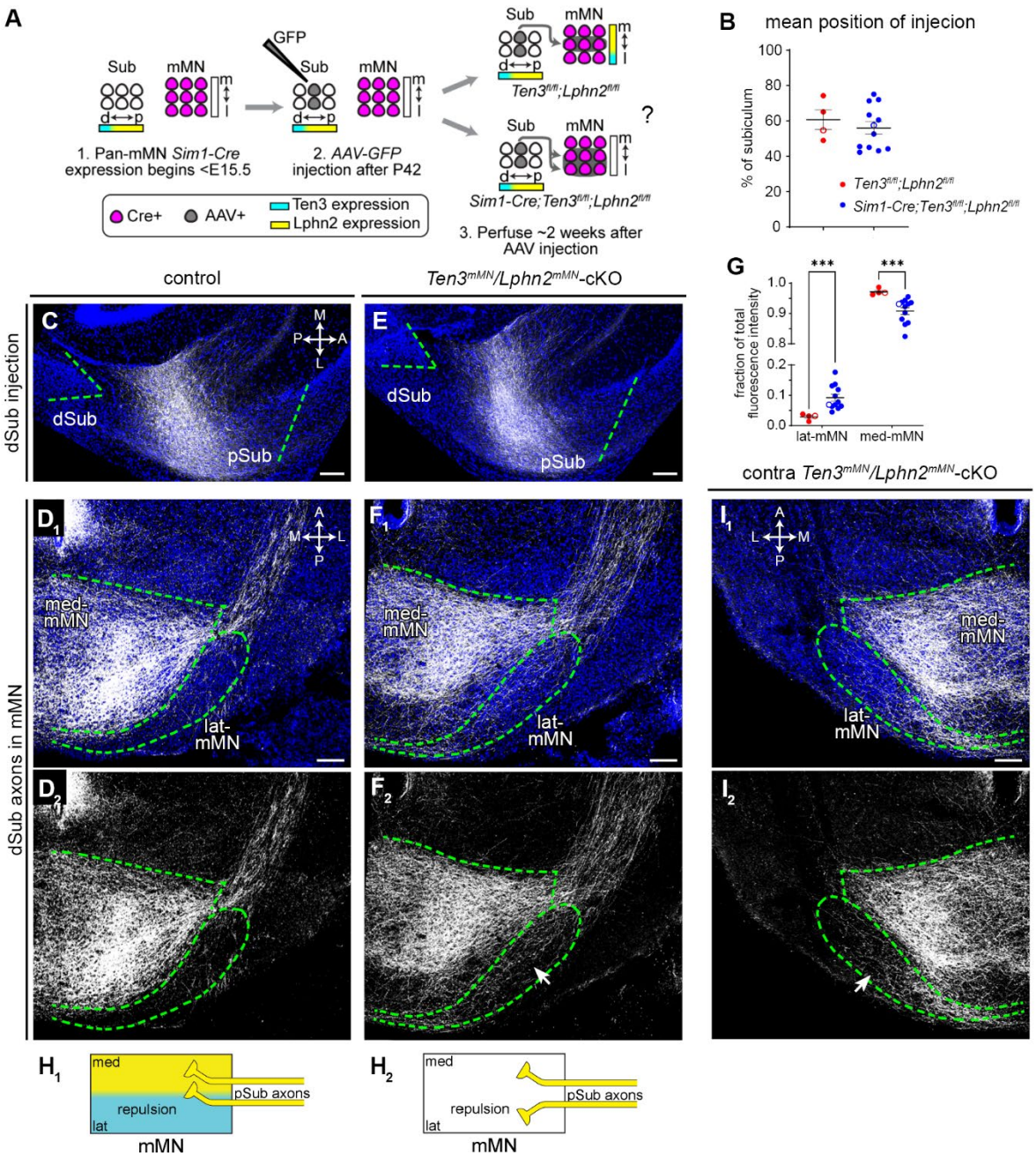

Figure 7. Ten3/Lphn2 are required in mMN for the precise targeting of pSub axons.

(A) Injection strategy and possible results for tracing pSub axons into mMN of *Ten3*$^{fl/fl}$*;Lphn2*$^{fl/fl}$ control (top right) and *Sim1-Cre;Ten3*$^{fl/fl}$*;Lphn2*$^{fl/fl}$ cKO mice (bottom right).

(B) Mean positions of injection sites along the distal→proximal axis of subiculum show no differences between *Ten3*$^{fl/fl}$*;Lphn2*$^{fl/fl}$ controls (n=4, red) and *Ten3*^{mMN}*/Lphn2*^{mMN}-cKO (n=12, blue). Open circles indicate representative animals shown in C, E. Mean ± SEM. Unpaired t-tests corrected for multiple comparisons (Holm-Šídák with Welch correction), no significant differences.

(C) Representative image of the *AAV-mCh* (gray) injection site of *Ten3*$^{fl/fl}$*;Lphn2*$^{fl/fl}$ controls show the virus is in pSub and pSub and does not reach dSub. Injection corresponds to animal in (D). Scale bar, 100 µm.

(D) Representative images of projection of pSub axons (gray) into mMN of *Ten3*$^{fl/fl}$*;Lphn2*$^{fl/fl}$ control mice (D_1). Bottom panel shows axons without DAPI counterstain (D_2). Scale bar, 100 µm.

(E, F) Same as C, D, but for *Ten3*^{mMN}*/Lphn2*^{mMN}-cKO mice. *Lphn2* cKO axons spread outside of med-mMN and into lat-mMN (arrow in F_2).

(G) Fraction of total projection intensity of pSub axons in lat-mMN (left) versus med-mMN (right) of the pSub (gray) axons of *Ten3*$^{fl/fl}$*;Lphn2*$^{fl/fl}$ *controls* (n = 4 mice, red) and *Ten3*^{mMN}*/Lphn2*^{mMN}-cKO (n = 12 mice, blue). Open circles indicate representative animals shown in D, F. Mean ± SEM. Unpaired t-tests corrected for multiple comparisons (Holm-Šídák with Welch correction), *** $p < 0.001$.
(H) Schematic summary of target selection of pSub axons in mMN of control (H_1) and *Ten3*^{mMN}*/Lphn2*^{mMN}-cKO (H_2) mice based on results in C–G.
(I) Same as F, but for projections into contralateral mMN. Contralateral Lphn2$^+$ axons spread outside of med-mMN and into lat-mMN of *Ten3*^{mMN}*/Lphn2*^{mMN}-cKO mMN (arrow in I_2).
Anatomical borders were drawn based on DAPI counterstain.
See Figures S3 for additional data. See Table S1 for detailed genotypes.

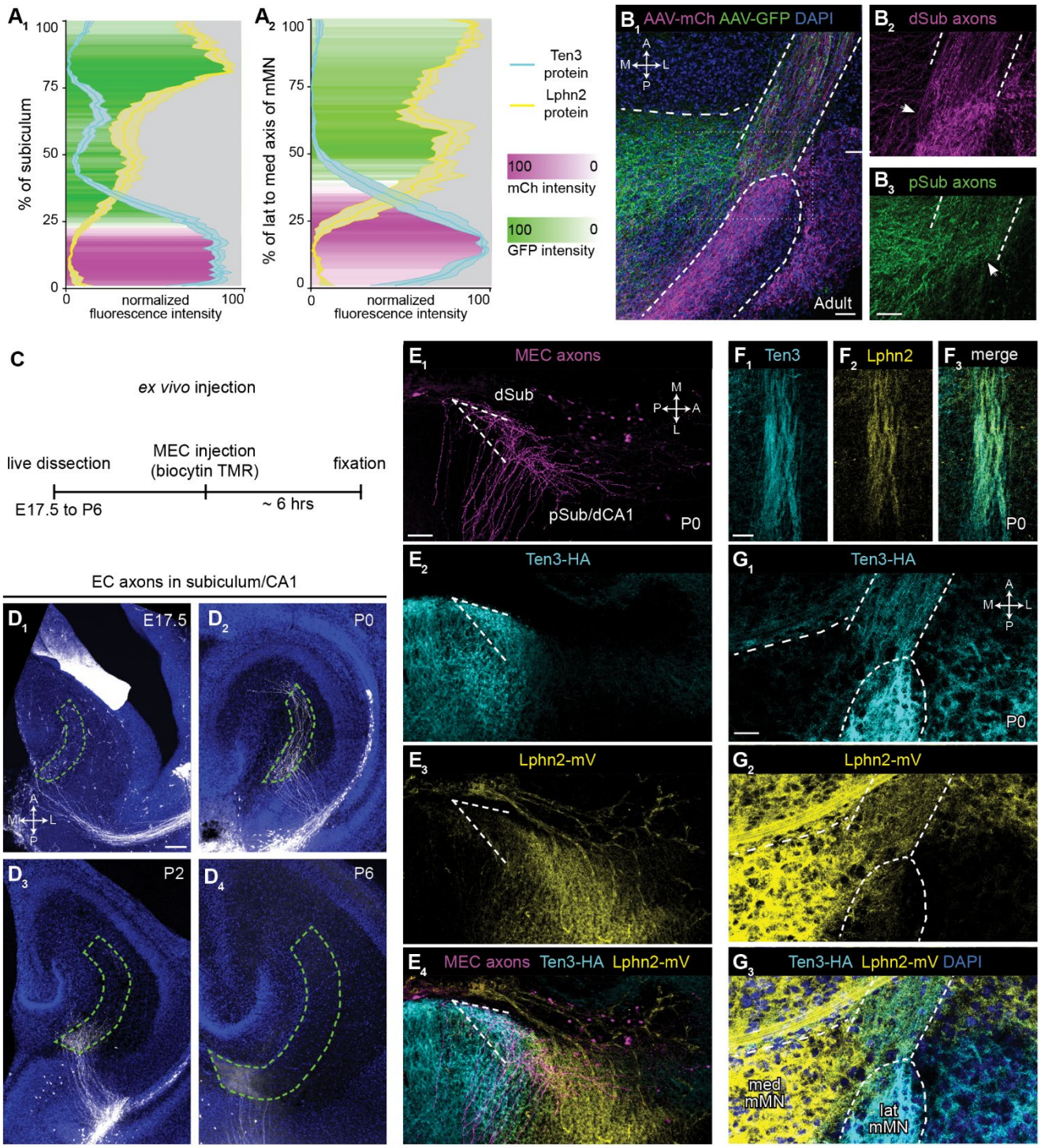

Figure S1. Timing and orientation of axon entry into targets

(A) Normalized fluorescence intensity traces of Ten3 (cyan) and Lphn2 (yellow) protein expression along the distal→proximal axis of subiculum overlaid with dSub (magenta) and pSub (GFP) injection site density heatmap (A_1) and a diagonal lat-mMN→med-mMN axis of mMN overlaid with density heatmap of projections from dSub (magenta) and pSub (GFP; A_2).

(B) Additional representative image of topographic projections in lat-mMN and med-mMN (B_1; from dual dSub and pSub injections), show axons do not segregate until reaching the target and then turn (arrows) to fill Ten3$^+$ (B_2) and Lphn2$^+$ subfields (B_3). Scale bar, 50 µm.

(C) Schematic for *ex vivo* injections for developmental tracing of entorhinal cortex→subiculum projection.

(D) Representative images of projection of entorhinal cortex axons into molecular layer of subiculum in wildtype animals at E17.5 (D_1), P0 (D_2), P2 (D_3), and P6 (D_4). Axons begin to invade subiculum at E17.5 and progressively increase in density through P6. Scale bar, 100 µm.
(E) Representative images of MEC axons (magenta) at P0 entering Ten3-high dSub (cyan) and turning before proceeding to Lphn2-high pSub (yellow) at P0. The three images are from the same confocal section showing axons (E_1), Ten3 protein (E_2), Lphn2 protein (E_3), and merge (E_4) channels. Scale bar, 50 µm.
(F) Representative images of subiculum axon tract at P0 along the path to mMN with extensive intermingling of $Ten3^+$ (cyan) and $Lphn2^+$ (yellow) axons in *Ten3*^{cTAG}*;Lphn2*^{mVenus} animals. The three images are from the same confocal section showing Ten3 (F_1), Lphn2 (F_2), and merge (F_3) channels. Scale bar, 50 µm.
(G) Representative images of subiculum axon tract at P0, entering mMN target where axons experience $Ten3^+$ and $Lphn2^+$ subfields simultaneously. Ten3 (cyan) and Lphn2 (yellow) axons remain intermingled in the tract up until terminal projections in the target. The three images are from the same confocal section showing Ten3 (G_1), Lphn2 (G_2), and merge (G_3) channels. Scale bar, 25 µm.

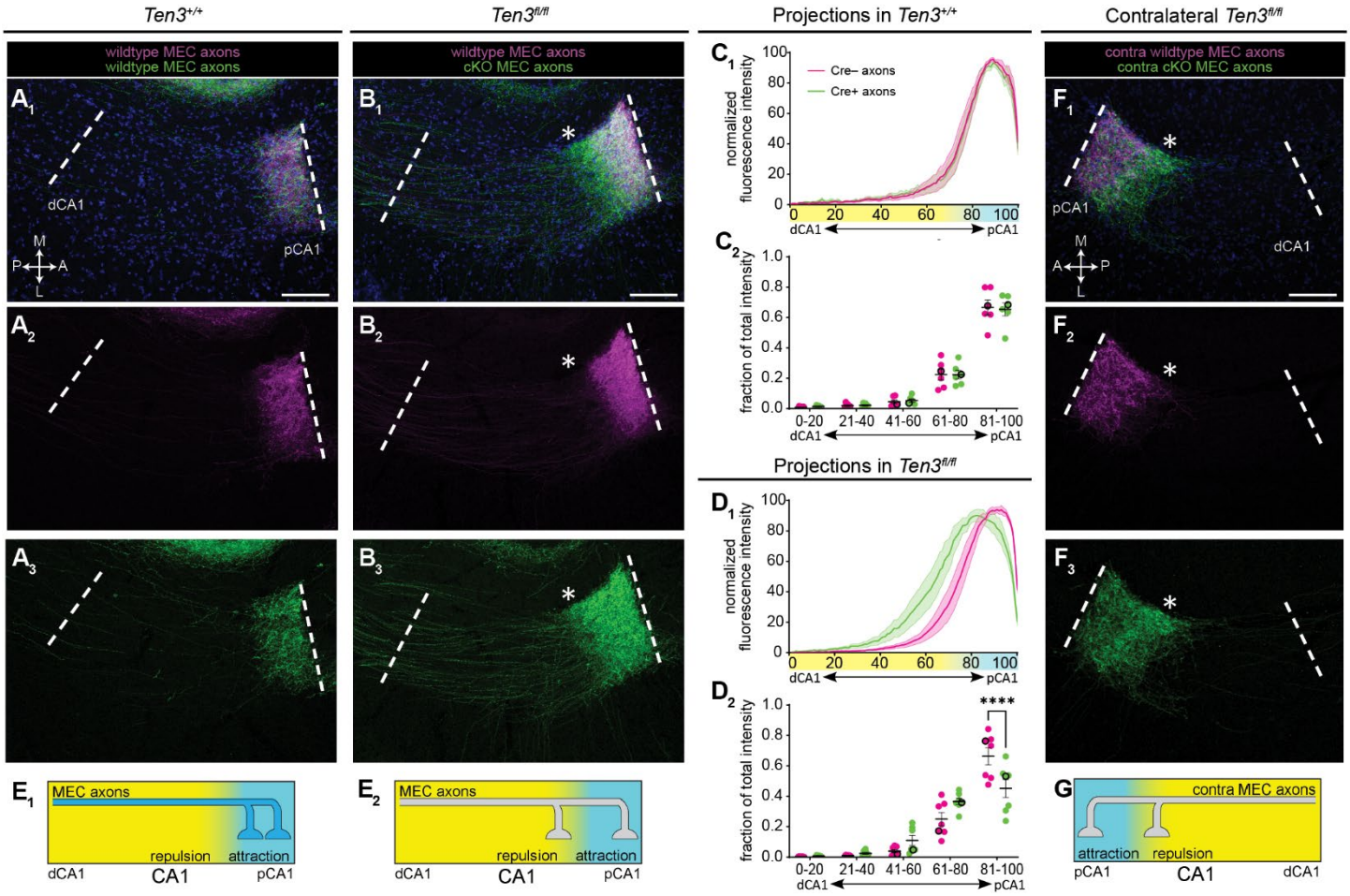

Figure S2. Additional analyses of the MEC axon projection, related to Figure 2

(A) Representative images of projection of Cre⁻ axons (magenta), and Cre⁺ axons (green) into molecular layer of CA1 in *Ten3*$^{+/+}$ controls. The three images are from the same confocal section showing merge (A_1), magenta only (A_2), or green only (A_3) channels. Corresponding injection site is shown in Figure 2C.

(B) Same as A but for *Ten3*$^{fl/fl}$ mice. *Ten3* cKO axons in *Ten3*$^{fl/fl}$ mice spread beyond the Cre⁻ control axons towards dCA1 (asterisk, in identical position across three images). Corresponding injection site is shown in Figure 2E.

(C_1) Normalized fluorescence intensity traces of the Cre⁻ (magenta) and Cre⁺ (green) projections along the distal→proximal axis of CA1 in *Ten3*$^{+/+}$ controls (n = 6 mice). Injection positions are shown in Figure 2B. Ten3 (cyan) and Lphn2 (yellow) expression is represented along the x-axis. Mean (dark line) ± SEM (shaded area).

(C_2) Fraction of total projection intensity (same as C_1) in 20% bins of CA1 axis of the Cre⁻ (magenta) and Cre⁺ (green) projections along the distal–proximal axis of CA1 in *Ten3*$^{+/+}$ controls (n = 6 mice). Injection positions are shown in Figure 2B. Black outlines indicate representative animal in A. Mean ± SEM. Two-way ANOVA corrected for multiple comparisons (Šídák correction), no significant differences.

(D) Same as C but for *Ten3*$^{fl/fl}$ (n = 7) mice. **** $p < 0.0001$.

(E) Schematic summary of target selection of MEC axons in CA1 in control (E_1) and *Ten3*^{MEC}-cKO (E_2) based on results in A–D.

(F) Same as B, but for projections into contralateral CA1. Contralateral Cre⁺, *Ten3* cKO axons in *Ten3*$^{fl/fl}$ mice spread beyond the contralateral Cre⁻ control axons towards dCA1 (asterisk, in identical position across three images). Corresponding injection site is shown in Figure 2K.

(G) Schematic summary of target selection of MEC axons in contralateral CA1 in *Ten3*^{MEC}-cKO mice.

Scale bars, 100 μm.

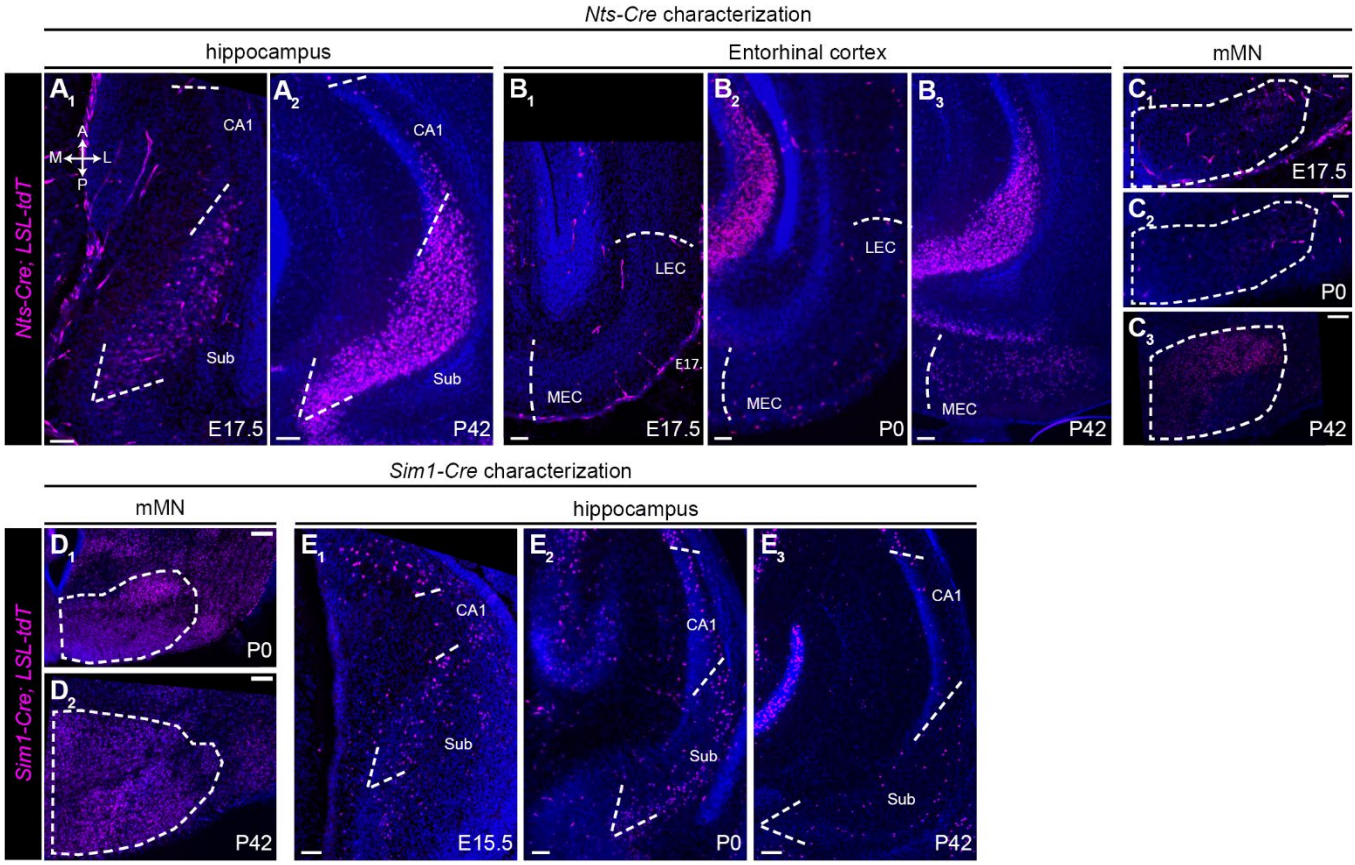

Figure S3. *Nts-Cre* and *Sim1-Cre* characterizations, related to Figures 3–7.

(A) Expression of *Nts-Cre* in subiculum and CA1, assessed by a nuclear tdTomato Cre reporter at E17.5 (A_1) and P42 (A_2). P0 data is in Figure 3A. The Cre reporter is sparsely expressed in subiculum at E17.5 and is denser by P0. Little CA1 expression is found even in adult. Scale bar, 50 µm (A_1), 100 µm (A_2).

(B) Same as A, except in entorhinal cortex with the addition of P0 (B_2). Expression is sparse in entorhinal cortex during development, ensuring target-only deletions in our examination of the MEC→dSub projection (Figure 3). Scale bar, 50 µm (B_1, B_2), 100 µm (B_3).

(C) Same as A, except in medial mammillary nucleus (mMN) with the addition of P0 (C_2). Expression is sparse in mMN during development, ensuring axon-only deletions in our examination of the subiculum→mMN projections (Figures 4 and 6). Scale bar, 50 µm (C_1, C_2), 100 µm (C_3).

(D) Expression of *Sim1-Cre* in mMN, assessed by a nuclear tdTomato Cre reporter at P0 (D_1) and P42 (D_2). E15.5 data is in Figure 5A. The Cre reporter is densely expressed in mMN by E15.5. Scale bars, 50 µm (D_1), 100 µm (D_2).

(E) Same as D, except in subiculum with the addition of E15.5 (E_1). Expression is sparse in subiculum during development and even in adults, ensuring target-only deletions in our examination of the subiculum→mMN projections (Figures 5 and 7). Scale bar, 50 µm (E_1, E_2), 100 µm (E_3).

All panels show endogenous tdTomato fluorescence, except for E17.5 *Nts-Cre* panels which are stained with RFP antibody (A_1, B_1, C_1).

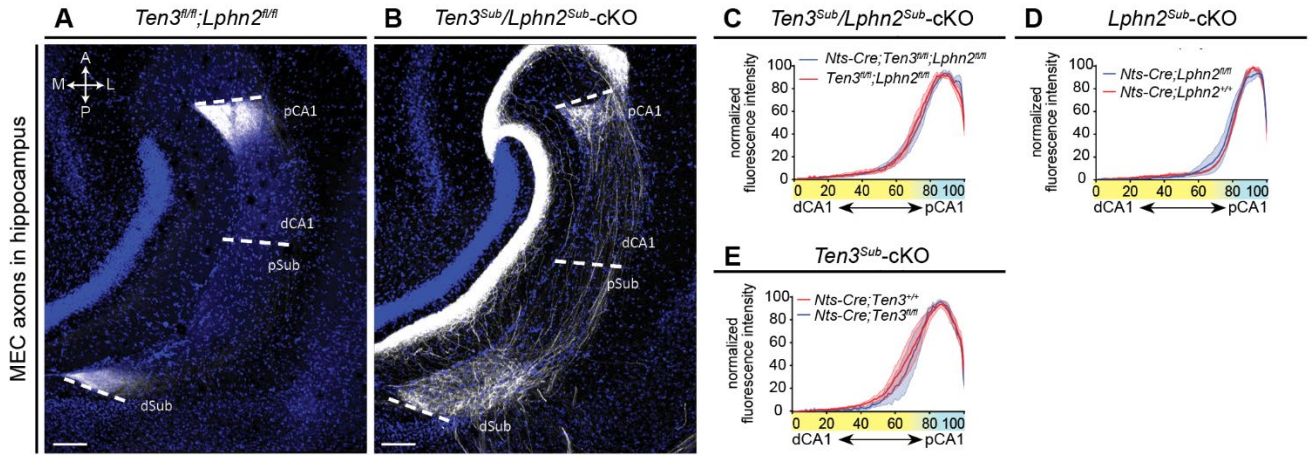

Figure S4. Normal targeting of MEC→pCA1 when in *Ten3/Lphn2* were conditionally knocked out in subiculum, related to Figure 3

(A) Representative image of MEC projections into molecular layer of CA1 and subiculum for *Ten*$^{fl/fl}$*;Lphn2*$^{fl/fl}$ controls. This is a larger field of view of Figure 3E to show that the same MEC axon population target both subiculum and CA1 with their terminals restricted to dSub and pCA1. Corresponding injection site is shown in Figure 2D. Scale bar, 100 µm.

(B) Same as A, but for *Nts-Cre;Ten3*$^{fl/fl}$*;Lphn2*$^{fl/fl}$ cKO mice. This is a larger field of view of Figure 3G$_1$. MEC axons spread towards pSub in subiculum but are restricted to pCA1 in CA1 as in control animals. Corresponding injection site is shown in Figure 2F.

(C) Normalized fluorescence intensity traces of MEC axon projections along the distal→proximal axis of CA1 internal controls in *Ten3*$^{fl/fl}$*;Lphn2*$^{fl/fl}$ mice (n = 7; red) and *Nts-Cre;Ten3*$^{fl/fl;}$*Lphn2*$^{fl/fl}$ mice (n = 5; blue). Injection positions are shown in Figure 3C. Ten3 (cyan) and Lphn2 (yellow) expression is represented along the x-axis. Mean (dark line) ± SEM (shaded area).

(D) Same as C, but for *Nts-Cre;Lphn2*$^{+/+}$ mice (n = 3; red) and *Nts-Cre;Lphn2*$^{fl/fl}$ mice (n = 5; blue).

(E) Same as C, but for *Nts-Cre;Ten3*$^{+/+}$ mice (n = 5; red) and *Nts-Cre;Ten3*$^{fl/fl}$ mice (n = 4; blue).

Together, these data indicate that conditional knockout of *Ten3/Lphn2* in subiculum does not affect MEC→pCA1 targeting precision.

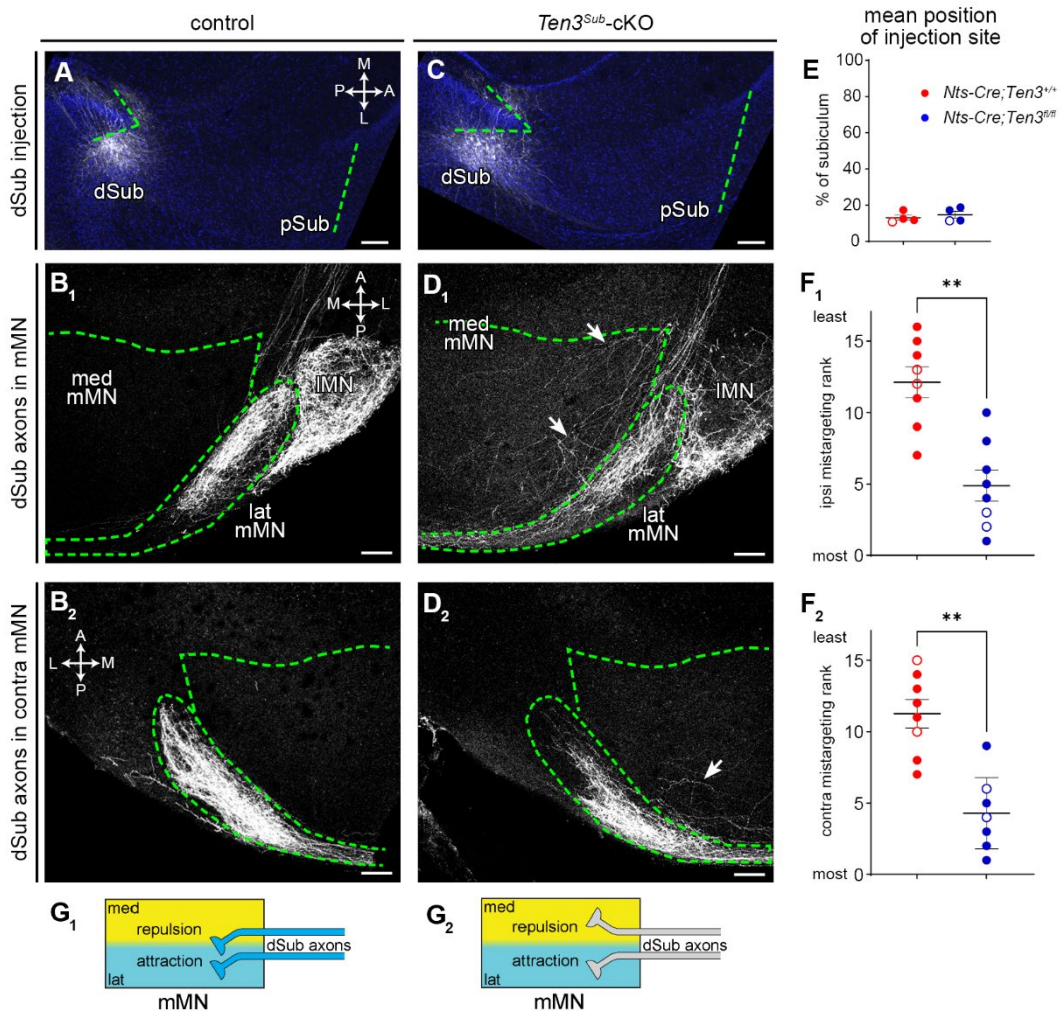

Figure S5. Additional *Ten3* axon deletion data to examine the dSub→lat-mMN projection, related to Figure 4.

In an independent set of experiments, we examined the phenotypes of dSub→lat-mMN projection in *Ten3*^{Sub}-cKO mice. Here, mistargeting of dSub axons into med-mMN in control and *Ten3*^{Sub}-cKO mice were rank-ordered by an experimenter blind to the genotype, based on the relative intensity of dSub axons in med-mMN and lat-mMN (to account for variations in injection intensity of anterograde tracers).

(A) Representative image of the *AAV-DIO-mCh* (gray) injection site of *Nts-Cre;Ten3*$^{+/+}$ controls show the virus is restricted to the most distal region of subiculum. Injection corresponds to animal in (B). Scale bar, 100 µm.

(B) Representative images of projection into ipsilateral (B_1) and contralateral (B_2) medial mammillary nucleus of *Nts-Cre;Ten3*$^{+/+}$ controls. Labeling in lateral mammillary nucleus (lMN) are unrelated axons from pre-subiculum. Scale bar, 100 µm.

(C, D) Same as A, B, but for *Nts-Cre;Ten3*$^{fl/fl}$ mice. Even the most distal subiculum axons show aberrant branches in med-mMN (arrows in D).

(E) Mean positions of injection sites along the distal→proximal axis of subiculum show no differences between *Nts-Cre;Ten3*$^{+/+}$ (red) and *Ten3*^{Sub}-cKO (blue). Open circles indicate representative image in A, D. Mean ± SEM. Unpaired t-test with Welch correction, no significant differences.

(F) Rank according to severity of mistargeting for *Nts-Cre;Ten3*$^{+/+}$ (red) and *Ten3*^{Sub}-cKO (blue) in ipsilateral (F_1) and contralateral (F_2) mMN. Open circles indicate representative animals in B, D. Ranked from most severe (1) to least severe (16). Mean ± SEM. Mann-Whitney U test, ** $P < 0.01$.

(G) Schematic summary of target selection of dSub axons in contralateral mMN of control (G_1) and *Ten3*^{Sub}-cKO (G_2) mice based on results in A–F.

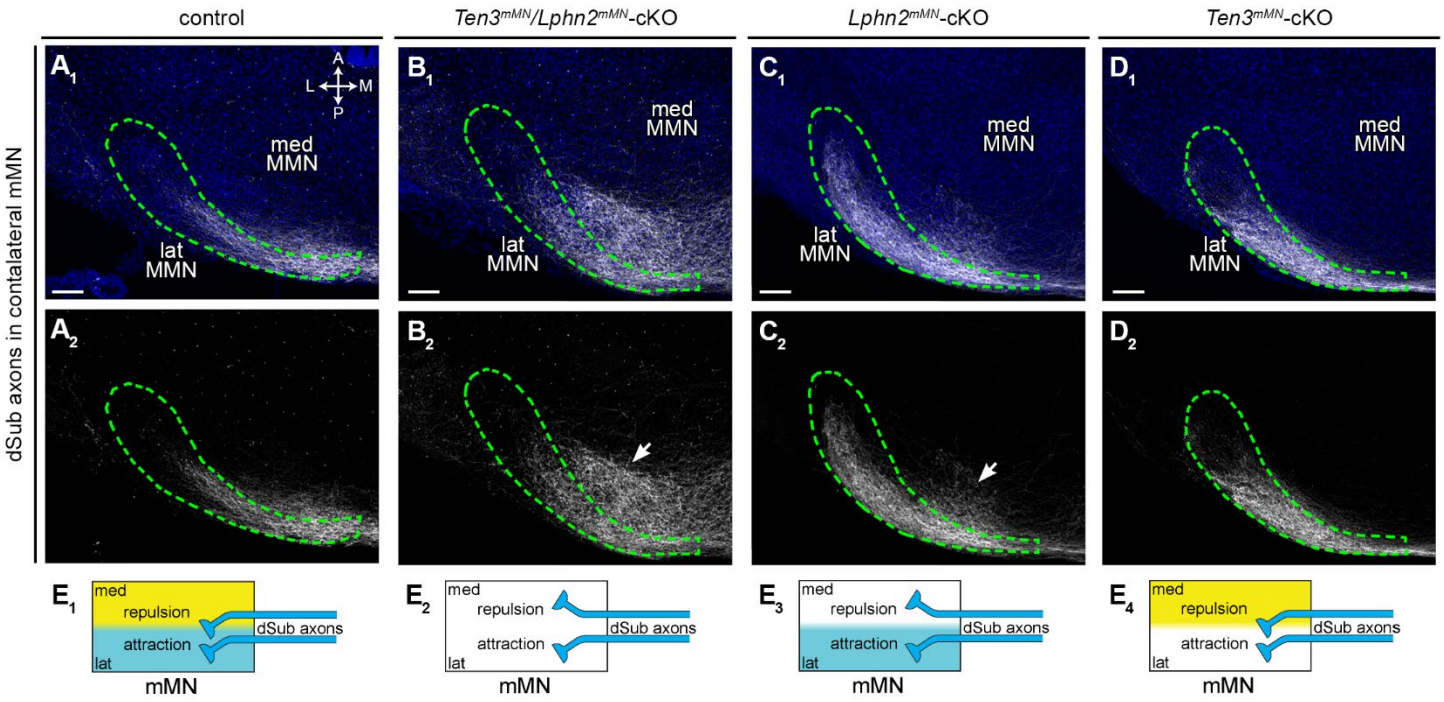

Figure S6. Analysis of contralateral dSub→lat-mMN projections in target deletion conditions, related to Figure 5

(A) Representative images of projection of dSub axons into contralateral medial mammillary nucleus of *Ten3*$^{fl/fl}$;*Lphn2*$^{fl/fl}$ control mice (A_1). Bottom panel shows axons without DAPI counterstain (A_2). Same animal as Figure 5D, E. Scale bar, 100 µm.

(B–D) Same as A, but for genotypes indicated above. dSub axons in *Ten3*^{mMN}/*Lphn2*^{mMN}-cKO (B) and *Lphn2*^{mMN}-cKO (C) mice spread medially outside of contralateral lat-mMN (arrows in B_2, C_2). Same as animal of corresponding genotype in Figure 5F–K.

(E) Schematic summary of target selection of dSub axons in contralateral mMN when *Ten3* (E_4), *Lphn2* (E_3), or both (E_2) were conditionally knocked out in mMN.

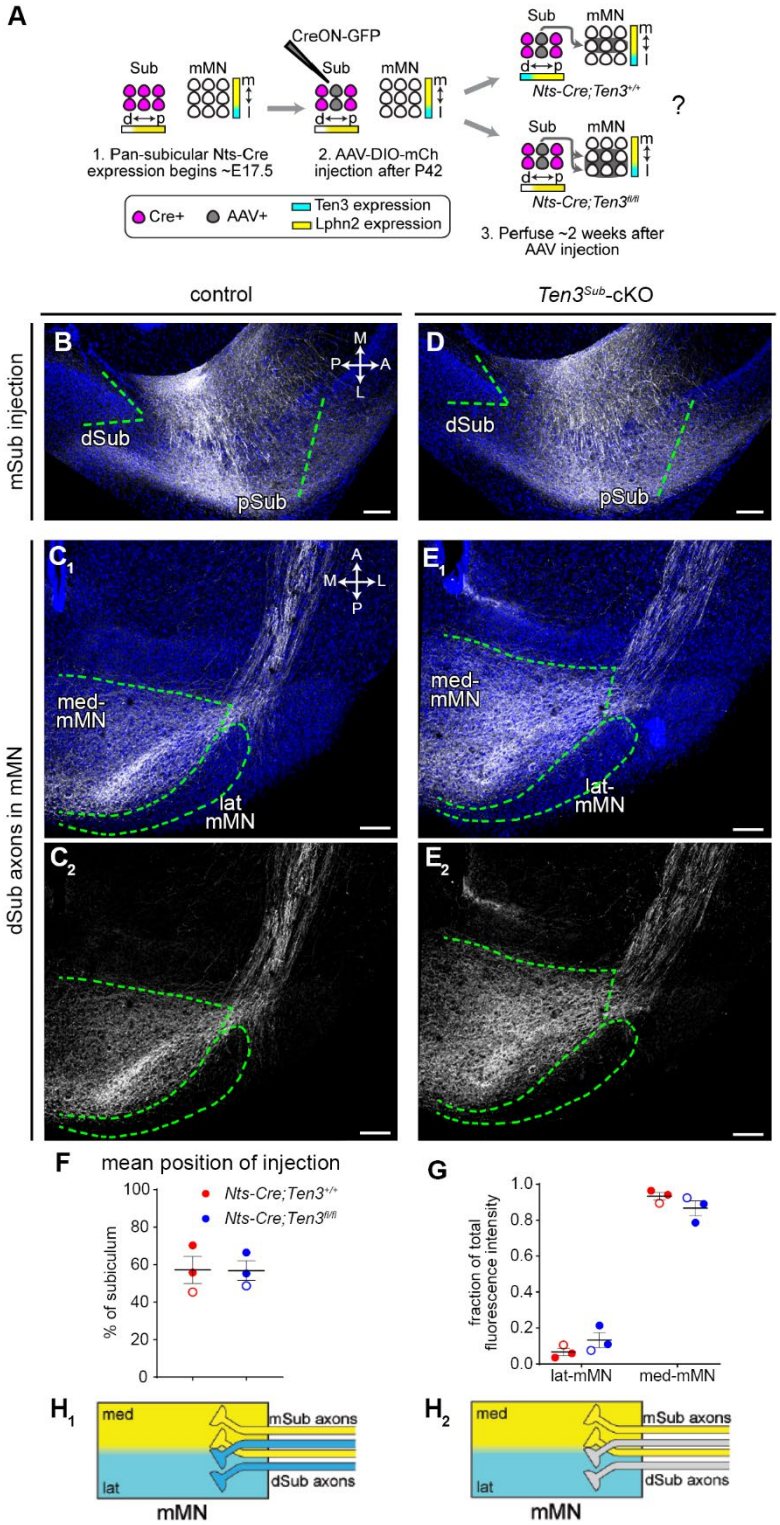

Figure S7. Lack of evidence for axon-axon interaction between Ten3$^+$ dSub and Lphn2$^+$ pSub axons in target selection at mMN, related to Figures 4 and 6.

Given that Ten3$^+$ dSub axons target to lat-mMN and Lphn2$^+$ pSub axons target to the adjacent med-mMN (Figure 1A), and dSub and pSub axons travel together from subiculum to mMN (Figure S1B, F, G), it is possible that Ten3 and Lphn2 could mediate axon-axon repulsion to sort dSub and pSub axons prior to reaching mMN, which could contribute to their target selection in mMN. The experiment here intends to test this possibility for the pSub→med-mMN projection (Lphn2$^+$) by deleting *Ten3* in subiculum.

(A) Injection strategy and potential results for tracing pSub (Lphn2^{+}) axons into medial mammillary nucleus (mMN) of *Nts-Cre;Ten3*$^{+/+}$ control (top right) and *Nts-Cre;Ten3*$^{fl/fl}$ mice (bottom right).
(B) Representative image of the *AAV-DIO-mCh* (gray) injection site of *Nts-Cre;Ten3*$^{+/+}$ controls show the virus is restricted to proximal region of subiculum. Injection corresponds to animal in (C). Scale bar, 100 µm.
(C) Representative images of projection of pSub axons (gray) into mMN of *Nts-Cre;Ten3*$^{+/+}$ controls (C_1). Bottom panel shows axons without DAPI counterstain (C_2). Scale bar, 100 µm.
(D, E) Same as B, C, but for *Nts-Cre;Ten3*$^{fl/fl}$. Lphn2^{+} pSub axon targeting is unaffected by *Ten3* deletion in subiculum axons.
(F) Mean positions of injection sites along the distal→proximal axis of subiculum show no differences between *Nts-Cre;Ten3*$^{+/+}$ controls (n = 3 mice) and *Ten3*^{Sub}-cKO (n = 3 mice). Open circles indicate representative animals in B, D. Mean ± SEM. Unpaired t-test with Welch correction, no significant differences.
(G) Fraction of total projection intensity in lat-mMN (left) versus med-mMN (right) of the pSub axons in *Nts-Cre;Ten3*$^{+/+}$ controls (red) and *Ten3*^{Sub}-cKO (blue). Open circles indicate representative animals in C, E. Mean ± SEM. Unpaired t-tests corrected for multiple comparisons (Holm-Šídák with Welch correction), no significant differences.
(H) Schematic summary of target selection of pSub axons in mMN of control (H_1) and *Ten3*^{Sub}-cKO (H_2) mice based on results in B–G.

				P0		Adult	
Figure	**Panel**	**Genotype**	**Designation**	**Region**	**Virus**	**Region**	**Virus/Tracer**
Figure 1	**B**	*Ten3$^{HA/HA}$;Lphn2$^{mVenus/mVenuss}$*	—	—	—	—	—
	C	wildtype	—	—	—	dSub pSub	*AAV8-ChR2-mCherry* *AAV8-ChR2-GFP*
Figure 2	**C–D**	CD1 wildtype	control (*Ten3$^{+/+}$*)	MEC	*LV-CAG-Cre-GFP*	MEC	*AAV8-CreON-GFP* *AAV8-CreOFF-mCherry*
	E–F, K–L	*Ten3$^{fl/fl}$*	*Ten3^{MEC}-cKO*	MEC	*LV-CAG-Cre-GFP*	MEC	*AAV8-CreON-GFP* *AAV8-CreOFF-mCherry*
Figure 3	**A**	*Nts-Cre;Ai75D/+*	*Nts-Cre;LSL-ntdT* [1]	—	—	—	—
	D–E	*Ten3$^{fl/fl}$;Lphn2$^{fl/fl}$*	control	—	—	MEC	*AAV8-CreOFF-mCherry*
	F–G	*Nts-Cre;Ten3$^{fl/fl}$;Lphn2$^{fl/fl}$*	*Ten3^{Sub}/Lphn2^{Sub}*-cKO	—	—	MEC	*AAV8-CreOFF-mCherry*
	H–I	*Nts-Cre;Ten3$^{+/+}$;Lphn2$^{fl/fl}$*	*Lphn2^{Sub}*-cKO	—	—	MEC	*AAV8-CreOFF-mCherry*
	J–K	*Nts-Cre;Ten3$^{fl/fl}$;Lphn2$^{+/+}$*	*Ten3^{Sub}*-cKO	—	—	MEC	*AAV8-CreOFF-mCherry*
Figure 4	**C–D**	*Nts-Cre;Ten3$^{+/+}$*	control	—	—	dSub	*AAV8-CreON-mCherry*
	E–F, I	*Nts-Cre;Ten3$^{fl/fl}$*	*Ten3^{Sub}*-cKO	—	—	dSub	*AAV8-CreON-mCherry*
Figure 5	**A**	*Sim1-Cre;Ai75D/+*	*Sim1-Cre;LSL-ntdT* [1]	—	—	—	—
	D–E	*Ten3$^{fl/fl}$;Lphn2$^{fl/fl}$*	control	—	—	dSub	*AAV8-ChR2-mCherry*
	F–G	*Sim1-Cre;Ten3$^{fl/fl}$;Lphn2$^{fl/fl}$*	*Ten3^{mMN}/Lphn2^{mMN}*-cKO	—	—	dSub	*AAV8-ChR2-mCherry*
	H–I	*Sim1-Cre;Ten3$^{+/+}$;Lphn2$^{fl/fl}$*	*Lphn2^{mMN}*-cKO	—	—	dSub	*AAV8-ChR2-mCherry*
	J–K	*Sim1-Cre;Ten3$^{fl/fl}$;Lphn2$^{+/+}$*	*Ten3^{mMN}*-cKO	—	—	dSub	*AAV8-ChR2-mCherry*
Figure 6	**C–D**	*Nts-Cre;Lphn2$^{+/+}$*	control	—	—	pSub	*AAV8-CreON-GFP*
	E–F, I	*Nts-Cre;Lphn2$^{fl/fl}$*	*Lphn2^{Sub}*-cKO	—	—	pSub	*AAV8-CreON-GFP*
Figure 7	**C–D**	*Ten3$^{fl/fl}$;Lphn2$^{fl/fl}$*	control	—	—	pSub	*AAV8-ChR2-GFP*
	E–F, I	*Sim1-Cre;Ten3$^{fl/fl}$;Lphn2$^{fl/fl}$*	*Ten3^{mMN}/Lphn2^{mMN}*-cKO	—	—	pSub	*AAV8-ChR2-GFP*
Sup. Figure 1	**C**	CD1 wildtype	—	MEC	Biocytin TMR[2]	—	—
	D	*Ten3$^{HA/HA}$;Lphn2$^{mVenus/mVenuss}$*	—	MEC	Biocytin TMR[2]	—	—
	E–F	*Ten3$^{HA/HA}$;Lphn2$^{mVenus/mVenuss}$*	—	—	—	—	—
Sup. Figure 2	**C–D**	CD1 wildtype	control (*Ten3$^{+/+}$*)	MEC	*LV-CAG-Cre-GFP*	MEC	*AAV8-CreON-GFP* *AAV8-CreOFF-mCherry*
	E–F, K–L	*Ten3$^{fl/fl}$*	*Ten3^{MEC}-cKO*	MEC	*LV-CAG-Cre-GFP*	MEC	*AAV8-CreON-GFP* *AAV8-CreOFF-mCherry*
Sup. Figure 3	**A–C**	*Nts-Cre;Ai75D/+*	*Nts-Cre;LSL-ntdT*	—	—	—	—
	D–E	*Sim1-Cre;Ai75D/+*	*Sim1-Cre;LSLn-ntdT*	—	—	—	—
Sup. Figure 4	**A**	*Ten3$^{fl/fl}$;Lphn2$^{fl/fl}$*	control	—	—	MEC	*AAV8-CreOFF-mCherry*
	B	*Nts-Cre;Ten3$^{fl/fl}$;Lphn2$^{fl/fl}$*	*Ten3^{Sub}/Lphn2^{Sub}*-cKO	—	—	MEC	*AAV8-CreOFF-mCherry*
Sup Figure 5	**A–B**	*Nts-Cre;Ten3$^{+/+}$*	control	—	—	dSub	*AAV8-CreON-mCherry*
	C–D	*Nts-Cre;Ten3$^{fl/fl}$*	*Ten3^{Sub}*-cKO	—	—	dSub	*AAV8-CreON-mCherry*
Sup. Figure 6	**A**	*Ten3$^{fl/fl}$;Lphn2$^{fl/fl}$*	control	—	—	dSub	*AAV8-ChR2-mCherry*
	B	*Sim1-Cre;Ten3$^{fl/fl}$;Lphn2$^{fl/fl}$*	*Ten3^{mMN}/Lphn2^{mMN}*-cKO	—	—	dSub	*AAV8-ChR2-mCherry*
	C	*Sim1-Cre;Ten3$^{+/+}$;Lphn2$^{fl/fl}$*	*Lphn2^{mMN}*-cKO	—	—	dSub	*AAV8-ChR2-mCherry*
	D	*Sim1-Cre;Ten3$^{fl/fl}$;Lphn2$^{+/+}$*	*Ten3^{mMN}*-cKO	—	—	dSub	*AAV8-ChR2-mCherry*
Sup. Figure 7	**B–C**	*Nts-Cre;Ten3$^{+/+}$*	control	—	—	pSub	*AAV8-CreON-GFP*
	D–E	*Nts-Cre;Ten3$^{fl/fl}$*	*Ten3^{Sub}*-cKO	—	—	pSub	*AAV8-CreON-GFP*

[1] ***LSL-****ntdT = CAG promoter-loxP-stop-loxP-nucleus-targeted tdTomato* in the *Rosa26* locus (a nuclear Cre reporter designated as *Ai75D*)

[2] Biocytin TMR [5-(and-6)-tetramethylrhodamine biocytin] was injected in several time points around birth, rather than exclusively P0

Table S1. Summary of genotypes and viruses in each experiment, arranged according to figure panel.

EXPERIMENTAL MODEL AND STUDY PARTICIPANT DETAILS

Mice

Protein expression and *ex vivo* injection experiments used Ten3$^{HA/HA}$; Lphn2$^{mVenus/mVenus}$ animals at postnatal day 0 (P0) and P8.[40,50.] CD-1 mice from Charles River Laboratories were used for double *in situ* hybridization and ex vivo tracing timeline experiments, ages ranging from embryonic day 15.5 (E15.5) to P6. All loss-of-function (LOF) experiments used crosses of *Nts-Cre* (C57BL/6 and 129/SvJ mixed background; JAX #017525),[58] *Sim1-Cre* (C57BL/6, 129/SvJ, and FVB mixed background; JAX #006395),[59] *Ten3$^{fl/fl}$* (mixed background C57BL/6, 129/SvJ, and CD1),[10] *Lphn2$^{fl/fl}$* (mixed background C57BL/6, 129/SvJ, and CD1).[50] Cre lines were characterized at E15.5, E17.5, P0 and adult using Ai75D nuclear reporter mice (*Rosa-CAG-LSL-ntdTomato::deltaNeo*; C57BL/6; JAX stock #025106).[60] Crosses used for each experiment are listed in detail in Table S1.

For the entorhinal cortex→subiculum and entorhinal cortex→CA1 Ten3 deletion in axons (CreON/CreOFF) experiments (Figure 2, Figure S2), breeder pairs were maintained to produce all homozygous litters due to the low probability of correctly injecting overlapped P0 lentivirus and adult AAVs. Thus, these animals were not randomly allocated to experimental groups and were instead compared to age-matched CD1 wildtypes. Randomly allocated littermate controls were used for all other loss-of-function experiments conducted at P42 or later.

Male and female mice were used for all experiments. Mice were group-housed on a 12 hr light/dark cycle with ad libitum access to food and water. All animal and virus procedures followed guidelines approved by Stanford University's Administrative Panel on Laboratory Animal Care and Administrative Panel on Biosafety in accordance with NIH guidelines.

Immunostaining

Animals were anesthetized with 2.5% Avertin (intraperitoneal) and transcardially perfused with 10 mM PBS, followed by 4% paraformaldehyde (PFA). Brains were dissected and post-fixed in 4% PFA for 1-2 hours (P0, P8) or 4-6 hours (>P42), then cryo-protected for at least 48 hours in a 30% sucrose solution. E15.5 and E17.5 brains for Cre characterizations (Figure S3) were fresh-dissected and post-fixed in 4% PFA overnight before cryoprotection. Brains were embedded in Optimum Cutting Temperature (OCT)-filled cryomolds in a 2-methylbutane bath, cooled by dry ice and stored at –80°C until sectioning. Serial 60 µm horizontal sections were collected free-floating in 24-well plates in a solution of 10 mM PBS and 0.02% sodium azide and stored at 4°C until staining. CD1 wildtype *ex vivo* injections were sectioned at 180 µm (See '*Ex vivo* injections' for more details). The staining procedure was as follows: Incubation in (1) 10 mM PBS for 3x 10 min washes at room temperature (RT), (2) blocking solution of 0.3% PBST and 10% normal donkey serum (NDS) for 1-2 hours RT, (3) primary antibody in 0.3% PBST for 2-3 nights at 4°C, (4) 0.3% PBST for 3x 10 min washes RT, (5) secondary antibody in 0.3% PBST and 10% NDS block for 1-2 hours RT, (6) DAPI (1:5000 dilution of 5 mg/mL; Invitrogen) in 0.3% PBST for 15 min RT, and (7) 10 mM PBS for 3x 10 min washes RT. Sections were mounted in 10 mM PBS and cover-slipped using ProLong Gold Antifade Mountant (Invitrogen). Primary antibodies include: Rabbit anti-HA (1:300, Cell Signaling #3724), Sheep GFP (1:1500, BioRad 4745-1051), chicken anti-GFP (1:1000, Aves Labs, GFP-1020), rat anti-mCherry (1:1000, ThermoFisher, M11217), rabbit anti-RFP (1:1000, Rockland 600-401-379), and guinea pig anti-Cre-recombinase (1:500, Synaptic Systems 257 005). Secondary antibodies used were species-specific conjugated antibodies: AlexaFluor 488 (1:1000, Invitrogen), Cy3 Affinipure (1:1000, Jackson ImmunoResearch), AlexaFluor 647 (1:1000, Invitrogen). Images were taken with a Zeiss LSM 900 confocal microscope. For quantification details see 'Image and data analysis…' sections.

Double *in situ* hybridization (RNAScope)

E15.5, E17.5, and P0 pups were sacrificed by rapid decapitation. For embryonic dissections, pregnant dams were anesthetized with isoflurane before cervical dislocation and uterine dissection. Brains were fresh-dissected in ice-cold 10 mM PBS and immediately embedded and frozen in OCT-filled cryomolds in a 2-methylbutane bath, cooled by dry ice. Brains were stored at –80°C until sectioning. Serial 12 µm horizontal sections were collected on Superfrost Plus slides (Fisher Scientific) and stored at –20°C until procedure. Double *in situs* were performed using the RNAscope Multiplex Fluorescent Reagent Kit v2 (ACD Bio)[41] and performed according to RNAScope

assay guidelines for fresh-frozen samples with the following modifications for neonatal tissue during pretreatment: Sections were fixed on slides for 90 minutes in 4% PFA and Protease III was used during the digestion step. Probes used were RNAScope Probe- Mm-Tenm3 (1:2, ACD Bio 411951) and RNAScope Probe-Mm-Lphn2-C2 (1:100, ACD Bio 319341-C2). Fluorophores used were Opal Dye 570 (1:1500, Akoya Biosciences) and Opal Dye 690 (1:1500, Akoya Biosciences). Images were taken with a Zeiss LSM 900 confocal microscope (10x objective, with 0.5x digital zoom).

Ex vivo injections

For embryonic dissections, pregnant dams were anesthetized with isoflurane before cervical dislocation and uterine dissection. Pups were sacrificed by rapid decapitation individually at the time of injection. Brains were fresh-dissected into ice-cold artificial cerebrospinal fluid (ACSF) that contained 15.3582 g choline chloride, 0.1864g KCl, 0.144 g NaH_2PO_4, 4.766 g HEPES, 0.99 g sodium ascorbate, 0.1522 g thiourea, 0.33 g sodium pyruvate, 0.111 $CaCl_2$, 0.1238 $MgCl_2$, 3 mL 7.5% $NaHCO_3$, 0.45 g glucose, and 2.5 g trehalose per 100 mL. A scalpel was used to crudely remove olfactory bulbs and the most rostral ~1/4 of the brain to create a flat surface as well as any midbrain and hindbrain structures obscuring the caudal surface of cerebral cortex. Brains were pinned with caudal surface exposed in a silicon-lined dissecting dish filled with ice-cold ACSF. Using exterior anatomy as a guide, 5% 5-(and-6)-tetramethylrhodamine biocytin in 0.9% saline (biocytin TMR; Invitrogen) was iontophoretically injected into the approximate location of medial entorhinal cortex. Iontophoresis was done for 3 min at 5 µA current using glass pipette tips with an outside diameter of 15–20 µm. Brains were then placed in carbogenated ACSF at RT for ~6 hours, covered to protect from light, to allow time for dye to spread to axon terminals. After 6 hours, brains were placed in 4% PFA overnight to fix and moved to 30% sucrose solution for 24-48 hours for cryoprotection. Brains were embedded, sectioned, and stained as described previously (See 'Immunostaining'), but were sectioned at 180 µm for axon tracing in wildtype animals to visualize more of the axon trajectory in one plane (Figure S1C, D).

Stereotactic injections in neonatal pups

Pups were anesthetized via hypothermia and mounted in stereotactic apparatus modified to hold them. Cranial anatomy was visualized through the skin for stereotactic coordinates and a small incision was created using a 27-gauge needle in place of a craniotomy. Stereotactic coordinates were measured from lambda. MEC coordinates were 2.05–2.15 mm lateral, 0.6–0.65 mm posterior, and 1.4–1.45 mm ventral from brain surface. 400 nL of *LV-CAG-Cre-GFP* (~6.6×10^8 copies/mL; SignaGen SL100283) was injected at 100 nl/min.

Stereotactic injections in adult mice

P42 or older mice were anesthetized using isoflurane and mounted in stereotactic apparatus. Virus was injected via iontophoresis (5 uA current, 7 s on/7 s off) for 2 min using glass pipette tips with an outside diameter of 10–15 µm. Mice were perfused 2-3 weeks post-injection and processed as described above (See 'Immunostaining'). Stereotactic coordinates are all measured from lambda and vary based on strain, genotype, and age. MEC coordinates were 2.75–3.1 mm lateral, 0.475–0.675 mm posterior, and 2.05–2.2 mm ventral from brain surface. Distal subiculum (dSub) coordinates were 2.8–2.9 mm lateral, 0.175 mm posterior to 0.05 mm anterior, and 1.95–2.05 mm ventral from brain surface. Medial subiculum (mSub) coordinates were 3.05–3.1 mm lateral, 0.2–0.525 mm anterior, and 1.95–2.05 mm ventral from brain surface. Viruses injected were as follows: *AAV8-EF1a-DIO-hChR2(H134R)-eYFP* (*CreON-GFP*; 2 $\times 10^{12}$–1×10^{13} copies/mL; Gene Vector and Virus core, Stanford University)[61], *AAV-EF1a-FAS-hChR2(H134R)-mCherry* (*CreOFF-mCh*; 2–8×10^{12}; Gene Vector and Virus core, Stanford University),[62] *AAV8-EF1a-DIO-hChR2(H134R)-mCherry-WPRE-HGHpA* (*CreON-mCh*; 4×10^{12}–1.2×10^{13} copies/mL; gift from Karl Deisseroth, Addgene viral prep # 20297-AAV8), *AAV8-hSyn-hChR2(H134R)-mCherry* (*AAV-mCh*; 1×10^{13} copies/mL gift from Karl Deisseroth, Addgene viral prep # 20297-AAV8), and *AAV8-Syn-ChR2(H134R)-GFP* (*AAV-GFP*; 1×10^{13} copies/mL; gift from Edward Boyden, Addgene viral prep # 58880-AAV8).[63]

Image and data analysis for entorhinal cortex→subiculum axon tracing

Images of injection sites (10x magnification) and projections (10x objective, with 0.45x digital zoom) were acquired for every other 60 µm section using a Zeiss LSM 900 confocal. Images of direction of axons entering subiculum at P0 were taken at 20x with 0.5x digital zoom (Figure S1E). Due to variations in injection sites and time lapse between experiments, exposures were adjusted for each mouse and fluorescence intensity was normalized post hoc for comparison. Fluorescence intensity and injection position measurements were done on unprocessed images and collected using FIJI. Data processing was performed in MATLAB and Excel.

Strict inclusion criteria were applied to ensure tracing only from the appropriate subnetwork (Ten3$^+$ MEC). Inclusion criteria were as follows: (1) Both AAV injection sites must be in medial entorhinal cortex (mean position within most medial 20% of entorhinal cortex)—based on Ten3 mRNA in horizontal entorhinal sections (Pederick 21); (2) lentivirus *Cre-GFP* injection must allow for roughly equal expression of *AAV-CreON-GFP* and *AAV-CreOFF-mCh;* (3) 3 brightest sections of *AAV-CreON-GFP* and *AAV-CreOFF-mCh* must overlap by 2 of 3 sections across the dorsal–ventral axis; (4) lentivirus Cre-GFP expression in subiculum and CA1 must be minimal. Animals that fulfilled these criteria were included in the quantifications reported in Figures 2, 3 and Figures S2, 4.

For injection site quantification, a 425-pixel-wide segmented line was drawn from medial to lateral of layer II/III entorhinal cortex using DAPI counterstain to define edges. The segmented lines from each channel in the image were straightened using the Straighten function. Background subtraction was done by measuring the mode value of background regions and using the Subtract function to remove the mode value. The Plot Profile command was then used to extract fluorescence intensity (FI) along the medial-lateral axis. To compare across animals, these FI plots were resampled into 100 equal bins representing the length of entorhinal cortex using a custom MATLAB code.[10,11] The FI traces of the three brightest sections of injection site were summed together and normalized to FI values of 0-100. The mean position of the injection site was calculated by multiplying the FI value by its bin position, summing across the entire axis, and dividing by the sub of FI values.

Because LV-Cre-GFP may extend past the *AAV-CreON-GFP* tracing injection, it contributes fluorescence that would influence the calculation for AAV injection mean position. To resolve this, all animals were stained with a Cre antibody in the far-red channel that was also processed as above. The image calculator function was used to subtract the Cre only channel from the GFP channel to remove any GFP being contributed by Cre-GFP before the Plot Profile was extracted.

Projection site processing and quantification was done similarly to the injection site quantification, but the initial line was drawn as a 50-pixel wide segmented line along the distal–proximal axis of subiculum molecular layer and a 100-pixel-wide segmented line along the distal–proximal axis of CA1 molecular layer. While it is impossible to avoid including axons occasionally traversing the space between subiculum and CA1, they are relatively uniform across genotype and account for only a small fraction of FI. Areas under the curve for subiculum FI traces were calculated in GraphPad Prism 10.

Image and data analysis for subiculum→mMN expression and topography

All images were acquired for every other 60-µm section using a Zeiss LSM 900 confocal (subiculum/mMN P8 Ten3–Lphn2 expression and adult subiculum injection site (10x objective, with 0.5x digital zoom); adult mMN projection site (10x objective, with 0.45x digital zoom)). Hippocampal-entorhinal image shown (Figure 1B) is at 10x magnification. Images of axon tract and direction of axons entering mMN at P0 were taken at 20x with 0.5x digital zoom (Figure S1F, G).

For subiculum P8 Ten3–Lphn2 expression quantification, a 150-pixel-wide segmented line was drawn along the distal–proximal axis of the subiculum cell body layer using DAPI counterstain to define edges. The segmented line was straightened, background subtracted, quantified, and the data processed as described for MEC injection above (See 'Image and data analysis for subiculum→mMN axon tracing'). Six sections from one animal (Figure 1B$_1$) are represented as Ten3 and Lphn2 fluorescence intensity traces (Figure S1A$_1$). For mMN P8 Ten3–Lphn2 expression quantification, a 250-pixel-wide segmented line was drawn along the Ten3–Lphn2 gradient (posterior-lateral to anterior-medial) and processed in the same way. Three sections from one animal (Figure 1B$_2$) are represented as Ten3 and Lphn2 fluorescence intensity (Figure S1A$_2$).

A 125-pixel-wide segmented line was drawn for adult subiculum injection site and a 250-pixel-wide segmented line was drawn for adult mMN projection site quantification. Both were processed as above, but a heatmap was generated in Prism 10 for opposing mCherry (dSub) and GFP (pSub) injection (FigureS1A_1) and projection site intensity (FigureS1A_2). Three sections from one animal (Figure 1C) are represented for each.

Image and data analysis for subiculum→mMN axon tracing

Images of injection sites (10x objective, with 0.5x digital zoom) and projections (10x objective, with 0.45x digital zoom) were acquired for every other 60-µm section using a Zeiss LSM 900 confocal. Due to variations in injection sites and time lapse between experiments, exposures were adjusted for each mouse and fluorescence intensity was normalized post hoc for comparison. Fluorescence intensity and injection position measurements were done on unprocessed images and collected using FIJI. Data processing was performed in MATLAB and Excel.

Strict inclusion criteria were applied to ensure tracing only from the appropriate subnetwork. Inclusion criteria for Ten3$^+$ dSub tracing is that AAV injection site must be in the most distal 20% of subiculum by mean position for sparse axon tracing (Figure S5) or between 12% and 20% for region-based analyses (Figures 4, 5). Animals that fulfilled these criteria were included in the quantifications reported in Figures 4, 5 and Figures S5, 6. Inclusion criteria for Lphn2$^+$ pSub are as follows: AAV injection site (1) must be between 40–80% of subiculum by mean position and (2) must have less than 10% of its total fluorescence within dSub (distal 20% of subiculum). Animals that fulfilled these criteria were included in the quantifications reported in Figures 6, 7 and Figures S7. These criteria are based on Ten3 and Lphn2 mRNA in horizontal subiculum sections.[11]

For injection site quantification, a 125-pixel-wide segmented line was drawn along the distal–proximal axis of the subiculum cell body layer using DAPI counterstain to define edges. The segmented line was straightened, background subtracted, quantified, and the data processed as described for MEC above (See 'Image and data analysis for subiculum→mMN axon tracing'), with the exception of Cre-related fluorescence subtraction.

For projection site quantification, regions of interests (ROIs) of lat-mMN and med-mMN were drawn using the DAPI counterstain to define edges. Background subtraction was done by measuring mean fluorescence intensity of background and using the Subtract function to delete it. The total fluorescence intensity of each ROI was collected using the raw integrated density measurement. Data is represented as the ratio of fluorescence intensity in lat-mMN or med-mMN over total fluorescence intensity in mMN.

Rank order data analysis for dSub→lat-mMN axon tracing

Imaging, inclusion criteria, and image and data processing for subiculum injection site is the same as above. Imaging and image processing for mMN projection is same as above (See 'Image and data analysis for subiculum→mMN axon tracing'). For rank order analysis, the total fluorescence intensity was collected from unprocessed images using the raw integrated density measurement in FIJI for each mMN. The two brightest ipsilateral and two brightest contralateral sections of mMN for each animal were auto-balanced using the brightness/contrast adjustment tool in FIJI to enhance the contrast of single axons. An independent researcher, blinded to genotype, numbered all ipsilateral and all contralateral images from most severe mistargeting (#1) to no mistargeting (#16), accounting for the amount of axons within the axon tract as a proxy for injection site density. Animals were re-identified and rank-sum statistics were performed (Figure S5).

Statistics

Statistical tests were performed using GraphPad Prism 10. For sample sizes and details of statistical analyses, see figure legends. All experiments were randomized, excluding the entorhinal cortex→subiculum, Ten3 deletion in axons experiment (See 'Mice' for more details).

ADDITIONAL REFERENCES

58. Leinninger GM, Opland DM, Jo YH, et al. Leptin Action via Neurotensin Neurons Controls Orexin, the Mesolimbic Dopamine System and Energy Balance. *Cell Metab*. 2011;14(3):313-323. doi:10.1016/j.cmet.2011.06.016

59. Balthasar N, Dalgaard LT, Lee CE, et al. Divergence of Melanocortin Pathways in the Control of Food Intake and Energy Expenditure. *Cell*. 2005;123(3):493-505. doi:10.1016/j.cell.2005.08.035
60. Quina LA, Harris J, Zeng H, Turner EE. Specific connections of the interpeduncular subnuclei reveal distinct components of the habenulopeduncular pathway. *J Comp Neurol*. 2017;525(12):2632-2656. doi:10.1002/cne.24221
61. Fenno LE, Mattis J, Ramakrishnan C, et al. Targeting cells with single vectors using multiple-feature Boolean logic. *Nat Methods*. 2014;11(7):763-772. doi:10.1038/nmeth.2996
62. Saunders A, Johnson C, Sabatini B. Novel recombinant adeno-associated viruses for Cre activated and inactivated transgene expression in neurons. *Front Neural Circuits*. 2012;6. doi:10.3389/fncir.2012.00047
63. Boyden ES, Zhang F, Bamberg E, Nagel G, Deisseroth K. Millisecond-timescale, genetically targeted optical control of neural activity. *Nat Neurosci*. 2005;8(9):1263-1268. doi:10.1038/nn1525

ACKNOWLEDGEMENTS
We thank the Neuroscience Gene Vector and Virus Core at Stanford University and SignaGen for producing and packaging custom viruses, T. Südhof for the *Lphn2*^{mVenus} and *Lphn2*^{floxed} mice, and members of the Luo lab, especially U. Chon, for advice and support. We thank T. Hindmarsh-Sten, A. Starr, Z. Li, K. Sangster, and A. Kania for critiques of the manuscript. E.C.G. was supported by National Institute of Mental Health, Ruth L. Kirschstein National Research Service Award (F31MH129079). D.T.P. was supported by an American Australian Association Education Fund Scholarship and the SFARI Fellows-to-Faculty Award (Simons Foundation). L.L. is an investigator at Howard Hughes Medical Institute. This work was supported by National Institutes of Health grant (R01-NS050580 to L.L.).

AUTHOR CONTRIBUTIONS
E.C.G. and D.T.P. conceptualized the study. E.C.G performed all of the experiments, except for the RNAscope assay (Figure 1D, E) which was performed by Y.Z. E.C.G. analyzed all data except for dSub→lat-mMN rank order sorting (Figure S5) which was performed by L.L.
E.C.G wrote the manuscript. L.L supervised the study and edited the manuscript.

COMPETING INTERESTS: The authors declare that they have no competing interests.

DATA AVAILABILITY: Data will be made available upon publication.

CODE AVAILABILITY: Code will be made available upon publication.